Neuroinflammation, Mitochondrial Defects and Neurodegeneration in Mucopolysaccharidosis III Type C Mouse Model

Carla Martins, M.Sc.[1*], Helena Hůlková, M.D.[2*], Larbi Dridi, Ph.D.[1], Virginie Dormoy-Raclet, Ph.D.[1], Lubov Grigoryeva, B.Sc.[1], Yoo Choi, B.Sc.[1], Alexander Langford-Smith, Ph.D.[3], Fiona L. Wilkinson, Ph.D.[3], Kazuhiro Ohmi, Ph.D.[4], Graziella DiCristo, Ph.D.[1]; Edith Hamel, Ph.D.[5], Jerôme Ausseil, Ph.D.[6], David Cheillan, M.D.[7], Alain Moreau, Ph.D.[1], Eva Svobodová, Ph.D.[2], Zuzana Hájková, Ph.D.[8], Markéta Tesařová, Ph.D.[8], Hana Hansíková, Ph.D.[8], Brian W. Bigger, Ph.D.[3], Martin Hrebícek, M.D.,[2] and Alexey V. Pshezhetsky, Ph.D.[1]

[1] CHU Ste-Justine, University of Montreal, Montreal, QC, Canada; [2]Institute of Inherited Metabolic Disorders, 1st Faculty of Medicine and General University Hospital in Prague, Charles University, Prague, Czech Republic; [3]Stem Cell & Neurotherapies, University of Manchester, Manchester; Centre de Biologie Humaine, Biochimie Spécialisée, [4]Department of Biological Chemistry, David Geffen School of Medicine, University of California Los Angeles, Los Angeles, California, United States of America, [5]Montreal Neurological Institute, McGill University, Montréal, QC, Canada; [6]CHU Amiens, and Unité INSERM U1088, UFR de Médecine, Université de Picardie-Jules Verne, Amiens, France; [7]Service des Maladies Héréditaires du Métabolisme et Dépistage Néonatal - Centre de Biologie Est, Hospices Civils de Lyon, Bron, France; [8]Department of Pediatrics, 1st Faculty of Medicine and General University Hospital in Prague, Charles University, Prague, Czech Republic.

* Equally contributed as the first authors

Alexey V. Pshezhetsky
Service de génétique médicale, CHU Sainte-Justine
3175 Côte Ste-Catherine, Montréal (QC) H3T 1C5 – Canada
E-Mail: alexei.pchejetski@umontreal.ca

Running Title: Pathophysiology of brain disease in MPS IIIC mouse

Abstract

Objective: Severe progressive neurological pediatric disease mucopolysaccharidosis III type C is caused by mutations in the *HGSNAT* gene leading to deficiency of acetyl-CoA: α-glucosaminide N-acetyltransferase involved in the lysosomal catabolism of heparan sulfate. To understand the pathophysiology of the disease we generated a mouse model of mucopolysaccharidosis III type C by germline inactivation of the *Hgsnat* gene.

Results: At 6-8 months mice showed hyperactivity, and reduced anxiety. Cognitive memory decline was detected at 10 months and at 12-13 months mice showed signs of unbalanced hesitant walk and urinary retention. Lysosomal accumulation of heparan sulfate was observed in hepatocytes, splenic sinus endothelium, cerebral microglia, liver Kupffer cells, fibroblasts and pericytes. Starting from 5 months brain neurones showed enlarged, structurally abnormal mitochondria, impaired mitochondrial energy metabolism, and storage of densely packed autofluorescent material, gangliosides, lysozyme, pTau, and beta amyloid.

Interpretation: Altogether, our data for the first time demonstrate that deficiency of acetyl-CoA: α-glucosaminide N-acetyltransferase causes lysosomal accumulation of heparan sulfate in microglial cells followed by their activation and cytokine release. They also show mitochondrial dysfunction in the neurones and neuronal loss explaining why mucopolysaccharidosis III type C manifests primarily as a neurodegenerative disease.

Keywords: glycosaminoglycans; mucopolysaccharidosis; heparan sulfate; acetyl-CoA: α-glucosaminide N-acetyltransferase; knockout mouse model.

Abbreviations: MPS = mucopolysaccharidosis; Hgsnat = acetyl-CoA: α-glucosaminide N-acetyltransferase**;** HS= heparan sulfate.

Introduction

Mucopolysaccharidosis III or Sanfilippo syndrome is a metabolic genetic disease caused by lysosomal accumulation of heparan sulfate (HS) (Neufeld and Muenzer, 2001; Valstar *et al.*, 2008). The disease includes four allelic subtypes caused by the genetic deficiencies of heparan N-sulfatase (MPS III type A; MIM #252900), α-N-acetylglucosaminidase (MPS III type B; MIM #252920), heparan sulfate acetyl-CoA: α-glucosaminide N-acetyltransferase or HGSNAT (MPS III type C; MIM #252930), and N-acetylglucosamine 6-sulfatase (MPS III type D; MIM #252940).

The majority of MPS IIIC patients have severe clinical manifestations with onset in early childhood. They rapidly develop progressive and severe neurological deterioration causing hyperactivity, sleep disorders, loss of speech, behavioral abnormalities, neuropsychiatric problems, mental retardation, hearing loss, visceral manifestations, such as mild hepatomegaly, mild dysostosis multiplex, mild coarse facies, and hypertrichosis (Bartsocas *et al.*, 1979). Most patients die before adulthood but some survive to the fourth decade with progressive dementia and retinitis pigmentosa (Neufeld and Muenzer, 2001; Ruijter *et al.*, 2008; Valstar *et al.*, 2008). The birth prevalence of MPS IIIC in Portugal and the Netherlands is 0.12 and 0.21 per 100,000, respectively (Pinto *et al.*, 2004; Poorthuis *et al.*, 1999).

HGSNAT transfers an acetyl group from cytoplasmic acetyl-CoA to terminal N-glucosamine residues of HS within the lysosomes(Klein *et al.*, 1978). To date, more than 80 *HGSNAT* mutations have been identified including 18 missense which all result in misfolding of the mutant enzyme(Feldhammer *et al.*, 2009)

Important insights into the physiological mechanism of MPS III have been obtained from studying animal models of the disease. Spontaneous avian(Aronovich *et al.*, 2001) and canine(Aronovich *et al.*, 2000; Ellinwood *et al.*, 2003) models of MPS IIIA and B and a caprine model of MPS IIID(Ginsberg *et al.*, 1999) have been described, but the majority of data has been obtained

by studying a knockout mouse model of MPS IIIB(Li *et al.*, 1999) and a spontaneous mouse model of MPS IIIA(Bhaumik *et al.*, 1999). Several mechanisms potentially underlying neurodegenerative process in MPS III were described. First, in both mouse models microglia cells are activated through interaction of their Toll-like receptor 4 (TLR4) with under-degraded HS fragments, as are astrocytes and the entire immune system in the brain(Ausseil *et al.*, 2008; DiRosario *et al.*, 2009; Ohmi *et al.*, 2003; Villani *et al.*, 2007). At the same time, inhibition of TLR4 signaling pathway in MPS IIIB mouse while delaying brain inflammation did not stop progression of the neurodegenerative process(Ausseil *et al.*, 2008). Second, storage of G_{M2} and G_{M3} gangliosides occurring in brain cerebral cortical and cerebellar neurons(McGlynn *et al.*, 2004) (Crawley *et al.*, 2006) was previously suggested to cause neuronal apoptosis in Tay-Sachs and Sandhoff diseases where G_{M2} ganglioside is accumulated due to genetic defects of hexosaminidases A and B, respectively (Huang *et al.*, 1997; Wada *et al.*, 2000). Interestingly, recently described double-mutant MPS IIIA and IIIB mice with a knockout GalNAc transferase crucial for the synthesis of gangliosides have significantly reduced lifespan and increased neurodegeneration as compared to the corresponding single-mutant MPS IIIA and MPS IIIB mice, suggesting that absence of gangliosides may also be deleterious in MPS III (Mohammed *et al.*, 2012). Third, neurodegeneration could be caused by protein aggregates(Ginsberg *et al.*, 1999; Hamano *et al.*, 2008; Ohmi *et al.*, 2009) detected in neurons of medial entorhinal cortex and the dentate gyrus and linked to impaired autophagy and/or increased extralysosomal level of HS proteoglycans, glypicans(Ohmi *et al.*, 2011). Fourth, stored HS fragments, which are in excess and abnormally sulfated in MPS IIIA and IIIB(Wilkinson *et al.*, 2012) can cause adverse signaling reactions in brain neurons inducing, in particular, overexpression of GM130 protein and subsequent alterations of the Golgi ribbon architecture(Roy *et al.*, 2012), enhanced proliferation and outgrowth of neurites(Hocquemiller *et al.*, 2010) as well as alteration of neural cell migration (Bruyere 2013, submitted) all potentially contributing to neuropathology.

However, it still remains to be determined which of the above mechanisms are important for the development of neuronal dysfunction and, therefore should be the target for the pharmaceutical intervention along with finding the ways to restore deficient HGSNAT activity in the patients' cells. It is also not understood whether the pathophysiological mechanism in all 4 subtypes of MPS III is the same despite different genetic and biochemical defects and severity of the clinical manifestation.

In the current work we report the generation of the first animal model of the MPS IIIC by inactivation of the *Hgsnat* gene in mice and present new pathological and mechanistic findings explaining the brain disease progression by the neuronal loss associated with mitochondrial dysfunction.

Subjects/Materials and Methods

Animals. Generation of C57Bl6 mice with targeted disruption of *Hgsnat* gene has been performed at Texas Institute for Genomic Medicine as previously described(Hansen *et al.*, 2008; Zambrowicz *et al.*, 2003). The heterozygous mice were crossed to C57BL/6NCrl strain distributed by Charles River Quebec or bred to each other and the litter genotyped by PCR as described below. The *Hgsnat-Geo* mice were compared with the appropriate age and sex-matching wild type controls. All mice were bred and maintained at the Canadian Council on Animal Care (CCAC)-accredited animal facilities of the CHU Ste-Justine Research Center according to the CCAC guidelines. Mice were housed in an enriched environment with continuous access to food and water, under constant temperature and humidity, on a 12 h light/dark cycle. Approval for the animal experimentation was granted by the Animal Care and Use Committee of the CHU Ste-Justine.

The genotypes of mice were determined using genomic DNA extracted from the clipped tail tip (see Extended Materials and Methods for sequences of primers and PCR conditions). A 463 and 297 bp fragments were amplified separately in wild type and *Hgsnat-Geo* homozygous mice, respectively, whereas both fragments were amplified in mice heterozygous for the *Hgsnat-Geo* allele.

Quantification of mouse *Hgsnat* mRNA and cytokines in mouse brain tissues was performed using a Stratagene Mx3000P QPCR System (see Extended Materials and Methods for sequences of primers and PCR conditions). Total RNA was isolated from cultured cells or mouse tissues using the Trizol Reagent (Invitrogen) according to the manufacturer's protocol and reverse-transcribed to cDNA using random primers and SuperScript III reverse transcriptase (Invitrogen). RLP32 mRNA was used as a reference control.

Neurological and behavioural examination of mice. The motor performance of mice was evaluated using a simplified neurological examination as previously described(Lema *et al.*, 2004). The rotating rod motor coordination test was performed using an accelerating 5-line Rotarod treadmill

for mice (3 cm in diameter). Animals (8 per age per genotype) were briefly trained at 4 rpm and tested using an accelerating mode (from 4 to 40 rpm over 5 min). Three trials separated by 20 min rest intervals were performed on 3 consecutive days. The open field test was performed by individually placing 2, 4, 6, 8, 10-month-old *Hgsnat-Geo*, or wild type mice into the center of an arena (40 cm length x 40 cm width x 50 cm height, white Plexiglas). Mouse behavior was recorded for one hour and analyzed using Top Scan software version 2.0 (Clever Sys. Inc., Reston, VA, USA). The path length, rapid exploratory behavior (speed > 100 mm/s), immobility (speed < 0.05 mm/s) as well as frequency, path length, duration and speed in the central (25%) area of the cage were analyzed. OFT was performed one hour into the mouse light cycle (Langford-Smith *et al.*, 2011a; Langford-Smith *et al.*, 2011b). A 30 min room adjustment period was implemented prior to the start of each test. All experiments were performed with a naïve group of 6 to10 animals by the same investigator (LG).

The 5, 7, 8 and 10-month-old mice (six per age per genotype) were subjected to the Morris Water Maze test for spatial learning essentially as described (Seyrantepe *et al.*, 2010). During a 3-day habituation period, mice were required to swim to a visible platform located in a selected quadrant of a circular (1.4 m in diameter and 34 cm high) tank filled with water (18±1°C). The escape latencies were measured and visual and motor acuity as well as motivation were tested. On the 4^{th} day, the water was made opaque with an inert paint, the platform was moved to a different quadrant and submerged (1 cm), the visual wall cues were switched and 5 days of hidden-platform testing ensued. Mice were given three trials of 90 s to find the platform (the maximum inter-trial interval was 45 min). On days 1 and 4, mice that could not find the platform in the allotted time were guided to and allowed to stay on it for 10 s. On day 9, following hidden-platform testing, all mice were given a 60 s probe trial in which the percentages of time spent and distance traveled in the target quadrant (no longer containing a platform), as well as the number of crossings over the previous location of the hidden platform were recorded, along with swimming speed. Escape latencies were acquired with the 2020 Plus tracking

system and Water 2020 software (Ganz FC62D video camera; HVS Image, UK). All experiments were started at the same time every day and performed by the same investigator (CM).

Analysis of glycosaminoglycans and gangliosides in mouse tissues. Total GAG and lipids were extracted from brain and liver tissues as previously described (Ausseil *et al.*, 2008). Briefly, frozen tissues were homogenized in water (10% v/w). Lipids were extracted by addition of 2 volumes of methanol and 1 volume of chloroform to one volume of the homogenate. After 10 min centrifugation at 1000 *g* the organic phase was collected, evaporated and used to analyse gangliosides. The pellet was re-suspended in 100 mM sodium acetate buffer pH 5.5, containing 5 mM cysteine, 5 mM EDTA and 1 mg/ml of papain, digested overnight at 65°C and cleared by centrifugation at 2500 *g* for 15 min. For the analysis of total GAG, 100 µl of the supernatant was added to 2.5 ml of dimethylmethylene blue reagent (Whitley *et al.*, 1989) and the absorbance at 535 nm was measured. GAG concentration (µg per mg of dried pellet) was calculated using purified HS standard.

Sphingolipids were extracted from the lipid fraction in the presence of deuterium-labeled standards (N-stearoyl (D^3)-monosialoganglioside G_{M2} and N-stearoyl (D^3)-monosialoganglioside G_{M3}, Matreya LLC, USA) by saponification(Kyrklund, 1987) and then fractionated and desalted using reverse-phase Bond Elut C18 columns. Samples were analyzed by direct flow injection at a rate of 200 µl/min on a triple-quadrupole mass spectrometer (API 3200 MS/MS; Sciex Applied Biosystems, Toronto, Canada) in the negative ionization mode using the multiple reactions monitoring (MRM) method. G_{M2} and G_{M3} species were measured separately. The concentrations of individual molecular species were calculated by comparing with the corresponding internal standards. Total G_{M2} and G_{M3} concentrations (pmol per mg of dried pellet) were calculated as sums of the concentrations of all molecular species.

Lysosomal enzyme assays. N-acetyltransferase, β-galactosidase, α-galactosidase and β-hexosaminidase activities in cellular and tissue homogenates were assayed using the corresponding

fluorogenic 4-methylumbelliferyl glycoside substrates as previously described(Seyrantepe *et al.*, 2008). Protein concentration was measured using a Bio-Rad Bradford kit.

Analysis of LC3 in the mouse brain tissues by Western blot. Total brains were homogenized in five volumes of 250 mM sucrose buffer containing 50 mM Tris-HCl pH 7.4, 1 mM EDTA and protease inhibitor cocktail using a Dounce homogenizer. Nuclei were cleared by centrifugation at 500 *g* for 10 min at 4°C. Supernatants were mixed with an equal volume of sucrose buffer containing 1% Triton X-100 and incubated for one hour at 4°C. Resulting lysates were centrifuged for 15 min at 13,000 *g* and supernatants separated by SDS-PAGE on 15% gels. Western blot analyses were performed according to standard protocols using anti-LC3 (Sigma, 1:2,000) and 12G10 anti-α-tubulin antibody (DSHB, 1:15,000). Equal protein loading was assured by Ponceau S staining. Signals were quantified using ImageQuant software.

Tissue processing for morphological studies. Animals were deeply anesthetized with sodium pentobarbital and perfused via intracardiac catheter with phosphate-buffered saline, pH 7.4 (PBS) followed by 4% paraformaldehyde in PBS. Brains and visceral organs were removed and immersed in 4% paraformaldehyde in PBS overnight. Tissues for light microscopy were trimmed, dehydrated with an ethanol series followed by acetone, acetone-xylene mixture and xylene and then embedded in paraffin. Tissues for fluorescent confocal microscopy were treated sequentially in 10%, 20% and 30% sucrose in PBS overnight at 4º C and embedded in OCT compound before freezing at -80º C. Tissues for electron microscopy were trimmed into small cubes, post-fixed with 1% osmium tetraoxide, dehydrated with an ethanol series and propylene oxide and embedded in Durcupan-Epon mixture.

Histopathology and immunohistochemistry. Four µm-thick sections of paraffin-embedded tissues were rehydrated with isopropyl alcohol, and then with 96%, 70%, and 60% ethanol. The sections were stained with either hematoxylin and eosin (H&E), or periodic acid-Shiff technique

(PAS), and a set of primary antibodies. In the latter case the sections were treated with 1% NaN_3 and 0.3% H_2O_2 for 10 min to inactivate endogenous peroxidase, blocked with 5% bovine fetal serum in PBS for 30 min (both at room temperature), and incubated with primary antibodies diluted in 5% bovine serum albumin in PBS overnight at 4°C. After staining with primary and secondary antibodies (see Extended Materials and Methods for the list of antibodies and their dilutions) sections were analyzed and photographed using a Nikon E800 equipped with Olympus digital camera (DP70). Autofluorescence of neurons was analyzed in unstained sections using fluorescence filter BV-2A (Ex 400-440 nm/DM 455/BA 470).

For fluorescent confocal microscopy 40 μm-thick sagittal sections were cut from OCT-embedded frozen brains using CM3050 S Microtome (Leica). The sections were treated with 1% Triton X-100, blocked with 10% goat serum in PBS and incubated overnight at 4°C with primary antibodies in 3% goat serum, 0.1% Triton X-100 in PBS followed by secondary antibodies (see Extended Materials and Methods for the list of antibodies and their dilutions). The slides were mounted with Vectashield mounting medium and analyzed using a LSM510 Meta Laser inverted confocal microscope (Zeiss, 63x oil objective, N.A. 1.4). Images were processed and quantified using the LSM image browser software (Zeiss) and Photoshop (Adobe).

Electron microscopy. Semi-thin sections were cut and stained with toluidin blue and viewed by light microscopy. The regions of interest for electron microscopy were selected and ultrathin sections were cut and mounted on 200 mesh copper grids. Sections were double contrasted with uranyl acetate and lead nitrate and then analyzed using a transmission electron microscope (JEOL 1200 EX).

Analyses of mitochondrial energy metabolism in mouse brain. Frozen brain tissues were homogenized at 4°C in 20 volumes of 50 mM Tris-HCl buffer pH 7.4, containing 150 mM KCl, 2 mM EDTA and 0.2 μg/ml of aprotinin. Mitochondria were isolated from the homogenate by differential centrifugation as described(Makinen and Lee, 1968). The activities of the mitochondrial

enzymes, NADH: ubiquinone oxidoreductase (NQR, complex I), succinate:CoQ reductase (SQR, complex II), ubiquinol:cytochrome c oxidoreductase (QCCR, complex III), cytochrome c oxidase (COX, complex IV), NADH:cytochrome c reductase (NCCR, complex I+III), succinate:cytochrome c reductase (SCCR, complex II+III) and citrate synthase (CS) were measured as described(Rustin *et al.*, 1994; Srere, 1969). Pyruvate dehydrogenase activity was determined as described (Dudkova *et al.*, 1995). Protein concentration was measured according to Lowry (Lowry *et al.*, 1951).

Total content of coenzyme Q10 in brain homogenate was determined as described(Mosca *et al.*, 2002) with minor modifications. 100 µl of brain homogenate was diluted with 100 µl of MilliQ H_2O. Mixture was supplemented with 50 µl of a 1,4-benzoquinone solution (2 mg/ml) and vortexed for 10 s. After 10 min 1 ml of n-propanol was added. The mixture was vortexed for 10 s and centrifuged at 10,000 rpm for 2 min. 50 µl of the supernatant was analyzed by HPLC using the Supelcosil LC 18 column (Supelco) eluted by ethanol/methanol (70/30 v/v) mixture at a flow rate of 1 ml/min. UV detection was performed at 275 nm. Results were expressed as pmol of Q10 per mg of total protein.

Quantitative analysis of neuronal density in the mouse brain cortex.

Four mice (2 male, 2 female) were studied for each age and genotype. For each brain, 3 sagittal sections, cut at 1.44, 1.68 and 1.92 mm lateral from bregma, (Paxinos and Franklin, 2013) were simultaneously stained with anti-NeuN antibodies as described above. For each section, 2 images of the S1 somatosensory cortex (S1Tr and S1HL for 1.44 and S1Tr and S1FL for 1.68 and 1.92 sections) were acquired using Nikon Eclipse E600 Epifluorescence Microscope (magnification 200x), Zeiss Axiocam 506 digital camera with the same settings for all sections. The acquired images were analyzed using Adobe Photoshop CS5 (Adobe Systems Inc., Mountain View, CA, USA). In each image, 2 rectangular fields with the area of 1.92 mm^2 were defined, on the right and left extremities of the photographed areas. The numbers of NeuN-stained neuronal nuclei for each field (12 fields for each

mouse) were counted by two non-biased observers blinded for the genotype, age and sex of the animals.

Results

1. Mice homozygous for *Hgsnat-Geo* allele show deficient *Hgsnat* mRNA and activity in tissues.

A functional knockout of the *Hgsnat* locus in C57Bl/6N mice was generated using gene trap technology as previously described (Hansen *et al.*, 2008; Zambrowicz *et al.*, 2003). A selectable marker β-geo, a functional fusion between the β-galactosidase-encoding gene and the *neo* gene from Tn5 encoding an aminoglycoside 3'-phosphotransferase, was inserted into the intron 7 of the *Hgsnat* gene leading to splicing of exon 7 into the β-geo cassette to generate a fusion protein containing Hgsnat amino acid sequence encoded by the exons 1-7 followed by aminoglycoside 3'-phosphotransferase and β-galactosidase (Fig. 1A). The *Btk* exon in the trap construct contained termination codons in all reading frames to prevent translation of the downstream *Hgsnat* exons (Fig. 1A).

Mice homozygous for *Hgsnat-Geo* allele (*Hgsnat-Geo* mice) were viable and born in the frequency expected from Mendelian inheritance (26 of the first 100) indicating that disruption of the *Hgsnat* gene did not cause embryonic lethality. Mice showed normal growth, were fertile and behaviorally indistinguishable from wild type or heterozygous animals until the age of 11 months.

Both expression of *Hgsnat* mRNA measured by RT-q-PCR (Fig. 1B) and the level of HGSNAT activity measured with fluorogenic substrate Muf-β-D-glucosaminide (Fig. 1C) in tissues and primary cultures of skin fibroblasts from the homozygous animals were reduced to 0.6-1.5% of that in wild type mice (below or close to detection limit of the method) confirming efficiency of the splicing outcome and validating the model biochemically. In the heterozygous mouse tissues HGSNAT activity was reduced to ~50% of wild type (Fig. 1C). In contrast, β-galactosidase activity measured in liver, kidney, brain, muscle and lung tissues of the *Hgsnat-Geo* mice at pH 7.5 was

significantly increased as compared to wild type mice (not shown) indicating that the Hgsnat-Geo fusion protein is produced but does not have N-acetyltransferase activity, which was expected because it is missing ~60% of the Hgsnat sequence including its predicted active site residue, His269 and 9 of 11 transmembrane domains presumably forming the AcCoA-transporting channel(Durand *et al.*, 2010)

Activities of other lysosomal glycosidases measured in the tissues of homozygous *Hgsnat-Geo* mice were either similar or higher than those in wild type mice and progressively increased with age of the animals suggesting augmented production of lysosomes previously described for the mouse models of other subtypes of MPS III and linked to lysosomal storage phenotype(Bhaumik *et al.*, 1999; Li *et al.*, 1999). In the *Hgsnat-Geo* mice the highest increase was observed in liver tissues where α-galactosidase activity was induced ~5 fold and β-hexosaminidase activity, ~20 fold by the age of 6 months (Fig. 1D). β-Hexosaminidase activity was also increased 2-3 fold in the brain, lungs and kidney suggesting that lysosomal storage occurs also in these tissues.

2. *Hgsnat-Geo* mice show reduced longevity, progressive behavioral changes and learning impairment.

No visible signs of illness were observed in the homozygous *Hgsnat-Geo* mice until the age of 11-12 months, when they showed weight loss, and abnormal gait. About 30% of animals at this age showed spasticity of hind limbs and loss of coordination in a balance test (supplemental video 1). At ~65 weeks of age mice presented signs of urinary retention resulting in abdominal distension absent in human patients but present in mouse models of both MPS IIIA and MPS IIIB (Li *et al.*, 1999) (Bhaumik *et al.*, 1999) and had to be euthanized (Fig. 2A). At all ages, heterozygous mice were clinically undistinguishable from their wild type siblings. No signs of skeletal abnormalities such as scoliosis reported previously in human patients or shortened scull with a “blunt” snout described in several MPS mouse models including those of MPS IIIA(Bhaumik *et al.*, 1999) were detected in the

homozygous *Hgsnat-Geo* mice by x-ray analysis (Fig. S1). Similarly, we did not detect any signs of femoral head necrosis also reported for human MPS III patients (de Ruijter *et al.*, 2013).

Neurological assessment (gait, posture, avoidance response, righting reflex, horizontal bar test, inverted wire screen test, all conducted on the group of 10 *Hgsnat-Geo* and 10 wild type by the same examiner blinded for the mouse genotype) was performed at 2 months, when MPS IIIA and B mice still show normal behavior and then repeated every 2 months with a naïve group of animals. Also every 2 months starting from the age of 4 months we studied motor activity using motor coordination test performed on an accelerating Rotarod treadmill for mice. Neither neurological assessment nor the accelerating Rotarod test (Fig. S2) revealed any signs of neuromuscular pathology in Hgsnat-deficient mice up to the age of 10 months.

In contrast, open field test performed 1 hour into their light cycle showed definite signs of increased activity and reduced anxiety including higher than average speed and distance travelled, increased frequency of crossing the central field and central distance traveled, as well as decreased frequency and duration of periods of immobility (Fig. 2B and supplemental video 2). The same trend was observed for both male and female mice but for female mice the differences with the control group became significant already at the age of 6 months whereas for male mice for most studied parameters the significant difference was observed only at 8 months. By the age of 10 months the signs of hyperactive behavior diminished resembling the trend observed in human MPS III patients (Fig. 2B).

Hippocampal function was assessed at 5, 7, 8 and 10 months using the Morris Water Maze test to measure memory and spatial learning capability. To make sure that Hgsnat-deficient mice had no visual or motor deficits that could affect the outcome of the test we accessed their ability to reach a visible platform in a 3 days pre-training test. We found that there were no differences between the mutant and wild type groups as Hgsnat-deficient and wild type mice of all age groups showed similar escape latencies in the visible platform testing (Fig. 2C). Learning progress of mutant mice at ages of

5, 7 and 8 months was similar to that of their wild type counterparts, as shown at the Fig. 2C for the 8-month-old group. In contrast, at the age of 10 months, Hgsnat-deficient mice needed significantly more time to find the hidden platform compared to their wild type counterparts, and to both wild type and mutant 8-month-old mice, suggesting impaired spatial learning. Additionally, in the probe trial on day 9 when the platform was removed, Hgsnat-deficient mice spent significantly less time and traveled less distance than wild type mice in the target quadrant where the platform used to be located, which indicated a decline of spatial memory (Fig. 2C). Moreover, 10-month-old mutant mice displayed lack of precision with less platform crossings compared to wild type counterparts, and to younger wild type and Hgsnat-deficient mice (Fig. 2C).

3. Pathological changes in tissues

Pathological examination of homozygous *Hgsnat-Geo* mice performed at the ages of 2, 4, 6, 10 and 11-12 months did not reveal any gross changes in the visceral organs and brains, except for the strikingly reduced abdominal fat detected at 11-12 months. The same animals usually also had largely distended bladder filled with 1–2 ml of urine consistent with urinary retention (Fig. S3). Microscopic examination however revealed multiple pathological changes in numerous tissues and organs already detectable at 2 months and progressively increasing with age.

Hepatocytes in the centrolobular and intermediate zones showed microvacuolization of cytoplasm, which became more prominent with age (Fig. S4A). Immunostaining with antibody against cathepsin D (CathD) detected expanded lysosomal system in hepatocytes compatible with lysosomal storage starting from 2 months (Fig. S4B). Kupffer cells are increased in number starting from 2 months and become enlarged and strongly stained for CathD at later stages, showing signs of transformation into foam cells (Fig. S4A-C). Besides Kupffer cells, liver sinusoids contained a sparse mixed inflammatory infiltrate. High-resolution analysis of liver tissues by electron microscopy revealed massive accumulation of vacuoles, either electron-lucent or containing a fine sparse material

characteristic of glycosaminoglycan (GAG) storage in the cytoplasm of hepatocytes and less prominent storage of this type in Kupffer and Ito cells (Fig. S4E-H).

In the spleen, storage dominated in splenic sinus endothelial cells (SSE) giving them an appearance resembling that of foam cells (Fig. S5). Population of macrophages in red pulp represented a mixture of small dendritic macrophages and slightly enlarged round cells containing autofluorescent lipopigment and corresponding to phagocytic phenotype. Macrophages in white pulp revealed mostly an inconspicuous stellate appearance. In general, there was no convincing presence in spleen tissue of macrophages with storage material even at the most advanced stages of disease (surviving 16-month-old mice). CathD immunostaining was compatible with lysosomal storage in SSE and was increased starting from 2 months (Fig. S5A). Electron-lucent storage vacuoles in SSE were also detected by electron microscopy (Fig. S5I).

Quantification of NeuN-stained neurons in the two selected areas of somatosensory cortex showed that neuronal loss in homozygous *Hgsnat-Geo* mice actually occurs starting from the age of 6 months and continues throughout the life resulting by the age of 12 months in the >30% reduction of neuronal density in these areas (Fig. 3A). In the cerebellar cortex, Purkinje cell loss was massive in the anterior lobe with lobules I, II and III most severely affected and lobules IX and X less affected at 12 months of age (Fig. S6). The number of GFAP-positive astrocytes and CD68-positive microglia cells became augmented starting from 4 months in all studied brain areas of the *Hgsnat-Geo* mice as compared with wild type mice and was further increased with age (shown for somatosensory cortex in Fig. 3B).

The most striking phenomenon observed in all parts of brain was a coarse vacuolization of the cytoplasm of multiple CD68-positive cells giving them foam cell-like appearance (Fig. 3C). These cells dispersed in gray and less so in white matter were frequently found adjacent to neurons suggesting that they represent perineuronal microglia. Individual macrophage-like CD68-positive cells with

cytoplasmic vacuoles were also detected in perivascular areas. Microglia cells containing storage materials were most prominent in caudatoputamen and in brain cortex. They were first detected in 2-month-old mice, thus preceding pathologic changes in neurons and become more frequent at later stages. Contrary to microglial cells, neurons were mostly featured by finely granular appearance of their perikarya without marked distension. The granular material accumulated in these neurons with a variable intensity was strongly PAS-positive (Fig. 3D) and displayed intense autofluorescence (Fig. 3E). Immunostaining with antibodies against CathD (Fig. 3F), revealed increased number and size of lysosomes in neurons of mutant mice. Neurons strongly stained with CathA were found in brain cortex, thalamus, hypothalamus, amygdala, midbrain, pons and cerebellum (Fig. S7). Accumulation of PAS-positive and autofluorescent materials was most prominent in neurons present in deep cortical layers, in hippocampus and in cerebellum. Neurons in caudatoputamen showed little involvement. Incipient neuronal storage was detectable in 5-month-old mice and widespread yet irregular neuronal storage was present in 12-month-old animals. No signs of lysosomal storage were detected in vascular endothelial cells (data not shown).

EM performed in brain cortex confirmed that neurons and microglial cells had two distinct types of storage (Fig. 4). Cortical microglia displayed prominent accumulation of electron-lucent storage vacuoles or those with a sparse fine content. In contrast, neuronal pathology was dominated by progressive lysosomal storage of electron-dense heterogeneous ceroid-like material and early detectable mitochondrial structural abnormalities. Mitochondria were pleomorphic and increased in number with many of them swollen with disorganized or reduced inner membranes. Storage in microglia was not accompanied by any structural mitochondrial changes. Storage compartments in neurons contained heterogeneous, granular and/or lamellar material, occasionally with lipid droplets. At the same time, EM of neurons did not reveal lysosomes containing classical zebra-bodies, but some storage deposits contained structures resembling degenerated mitochondria. At the most advanced

stages of the disease (14-16 months), ultrastructural pattern in neuronal lysosomes was dominated by massive accumulation of closely packed fibrillary deposits often resembling storage material of a rectilinear and/or fingerprint type in neuronal ceroid lipofuscinoses (Fig. 4).

Other studied mouse organs and tissues stayed generally unaffected even at 12 months of age except for urinary bladders, which were markedly distended with thin walls. A sparse presence of cells strongly stained for CathD and presumably having lysosomal storage was detected in lamina, muscularis propria and adventitia. Normally arranged cardiomyocytes without regressive changes were observed in heart. There was no fibrosis in the interstitium and interstitial elements did not show signs of lysosomal storage at the optical level. Similarly, lysosomal storage was not detectable in alveolar septa in lungs. Population of septal and alveolar macrophages was rich, with focally increased phagocytic activity and undistinguishable from that seen in wild type. Respiratory bronchial epithelium displayed increased staining for CathD suggestive of lysosomal storage. In kidney, increased immunostaining for CathD was detected in glomeruli and in epithelial cells of distal tubules and collecting ducts (Fig. S5E). Storage of electron-lucent vacuoles in fibroblasts, vascular pericytes and rarely in vascular endothelial cells was detectable at the ultrastructural level (Fig. S5J-L).

4. *Hgsnat-Geo* mice show lysosomal GAG storage in neurons and microglial cells and ganglioside storage in non-lysosomal compartments of neurons

To investigate if Hgsnat deficiency in mouse tissues resulted in impairment of heparan sulfate catabolism, total GAG in mouse brain and liver tissues were measured at the age of 2, 4, 6, 8, 10 and 12 months (Fig. 5A). In both tissues GAG levels were slightly increasing with age while remaining significantly higher than in the wild type mice (on average two fold increase in brain and almost ten fold increase in liver at 12 months). At the same time, total GAG in brain tissues of *Hgsnat-Geo* mice at all ages was significantly lower than in MPS IIIB mice.

GAG accumulation at the cellular level was studied by immunohistochemistry using monoclonal 10E4 antibody specific against a native HS epitope (David *et al.*, 1992), which detected increased staining of cytoplasmic LAMP-1-positive organelles in multiple cells throughout somatosensory cortex and all regions of hippocampus. The lysosomal HS storage was detected in multiple NeuN-positive neurons, but even more intense 10E4 staining was detected in the cells negative for NeuN, but positive for the markers of activated microglia cells: Alexa 568-labeled isolectin B4 (ILB4), and CD68 (Fig. 5B).

Tandem mass spectrometry demonstrated ~2 fold increased levels of G_{M2} and G_{M3} gangliosides in the brain tissues of 4-month-old *Hgsnat-Geo* mice as compared to their wild type siblings (Fig. 5C), consistent with previously reported storage of these lipids in the mouse models of MPS IIIA and B(Bhaumik *et al.*, 1999; Li *et al.*, 1999). Accumulation of gangliosides in brain tissues was further studied by immunohistochemistry using the human-mouse chimeric monoclonal antibody, KM966(Nakamura *et al.*, 1994) specific to G_{M2} ganglioside(Huang *et al.*, 1997) and mouse monoclonal antibody specific to G_{M3} ganglioside. Both gangliosides, almost undetectable in the brain of wild type mice (Fig. S8) were highly present in the brains of *Hgsnat-Geo* mice (Fig. 5D). The ganglioside storage was observed in most areas of the brain, including the cerebellum, but was more prominent in deep layers of cortex and hippocampus (Fig 5D and Fig. S8).

All ganglioside-accumulating cells were recognized by the anti-NeuN antibody and were not stained with ILB4 indicating that they are neurons but not microglial cells (Fig. 5D). In contrast to GAG accumulation both the number of ganglioside-positive granules in the neurons and their size were dramatically increasing between the ages of 8 and 12 months (Fig. S8). Intriguingly, when the tissue sections were co-stained for both G_{M3} and G_{M2} gangliosides, we detected only modest level of co-localization indicating that the corresponding storage granules tend to segregate from each other (Fig. 5D). Similar pattern was previously observed in MPS IIIA and B mouse models (McGlynn *et*

al., 2004). Also, we observed only partial co-localization between the stored gangliosides and lysosomal marker LAMP-1 (Fig. 5D), which could indicate that the gangliosides are accumulated in the compartments having both lysosomal and non-lysosomal origin.

When we, however, co-stained the cells for gangliosides and the mitochondrial marker cytochrome c oxidase subunit 4 (Cox4) we detected a high degree of co-localization (Fig. 5D) suggesting that some of the storage granules could appear in the result of impaired mitophagy also consistent with the results of the EM analysis of neurons (as described above). Cox4 staining also revealed that the mitochondrial network is less organized and the ratio between the fused and single mitochondria is reduced in the tissues of the mutant mice (Fig. S9).

5. Brain tissues of *Hgsnat-Geo* mice show altered autophagy, impaired proteolysis and accumulation of missfolded proteins.

Impaired autophagy associated with decreased lysosomal and proteosomal proteolysis was found to be a characteristic feature of cells in many lysosomal disorders (Bifsha *et al.*, 2007), (reviewed in(Settembre *et al.*, 2013)). To test whether it is also the case for liver and brain tissues of Hgsnat-deficient mice we have analyzed the relative abundance of the two forms of light chain three protein (LC3). During the formation of the autophagosome a cytosolic form of LC3 (LC3-I) is cleaved and conjugated with phosphatidylethanolamine to form the LC3-phosphatidylethanolamine conjugate (LC3-II) tightly associated with the autophagosomal membranes, so the amount of LC3-II or the presence of LC3-positive punctate in the cytoplasm reflects the existence of autophagosomes. In liver tissues of *Hgsnat-Geo* mice the increased levels of the LC3-II were detected at all ages indicating increased autophagosomal genesis or decreased macroautophagic flux (Fig. S10). In the brain, the increase of LC3-II was also detected, but only at the age of 6 months and older (Fig. 6A).

The results of Western blot were consistent with the results of immunohistochemistry that showed presence of LC3 in the cytoplasm of medial entorhinal cortex (MEnt) neurons at 10 months

of age (Fig. 6B). We also detected drastically increased neuronal levels of SCMAS (subunit C of mitochondrial ATP synthase) aggregates and ubiquitin suggestive of mitophagy and a general impairment of proteolysis. We also detected increased levels of O-GlcNAc-modified proteins, an indication of the ER stress often associated with impaired cellular proteolysis(Chatham and Marchase, 2010) (Fig. 6C)

Recent studies have demonstrated that neurons in certain brain areas of MPS IIIB and MPS IIIA mice, primarily dentate gyrus and MEnt involved in learning and memory have increased levels of protein markers of Alzheimer disease and other tauopathies leading to dementia such as lysozyme, hyperphosphorylated tau (Ptau), Ptau kinase, Gsk3β, and beta amyloid(Ohmi *et al.*, 2009; Ohmi *et al.*, 2011). All these markers are also increased in the brains of Hgsnat-deficient mice (Fig. S11) although their levels are somewhat lower than those in the MPS IIIA and MPS IIIB mice of similar age (Ohmi *et al.*, 2011).

6. Mitochondrial energy metabolism is compromised in brain tissues of *Hgsnat-Geo* mice

To verify whether mitochondrial energy metabolism is affected in the brain cells of *Hgsnat-Geo* mice we have measured activities of several mitochondrial respiratory chain enzymes including NADH:CoQ reductase (NQR, complex I), succinate:CoQ reductase (SQR, complex II), cytochrome c oxidase (COX, complex IV), NADH:cytochrome c reductase (NCCR, complex I+III), succinate:cytochrome c reductase (SCCR, complex II+III) in the isolated brain mitochondria. We also measured activities of pyruvate dehydrogenase (PDH) complex and citrate synthase (CS).

Activities of complex IV (COX) and complex II (SQR) enzymes were significantly lower in *Hgsnat-Geo* mice than in the corresponding wild type controls at the ages of 8 and 12 months and 8 months, respectively (Fig. 7A). No significant differences in activities of enzymes of complex I, complex I+III, complex III, and complex II+III of respiratory chain as well as PDH and control

mitochondrial enzyme citrate synthase (CS) were found between *Hgsnat-Geo* and wild type mice. However, when we analyzed the activities of individual enzymes as a function of mouse age, we found that the activities of complex II (SQR), complex II+III (SCCR) and citrate synthase in *Hgsnat-Geo* mice decreased significantly with age, whereas no dependence was detected for the wild type animals (Fig. 7B).

Consistent with the gradual reduction of the activities of respiratory chain enzymes was the observed decrease of the total content of coenzyme Q10 in the brain tissues of *Hgsnat-Geo* mice. At the age of 4 months the levels of Q10 in the wild type and Hgsnat-deficient mice were the same, but while in the wild type mice of older age Q10 stayed at the same level; in the brains of *Hgsnat-Geo* mice it showed a negative correlation with age and at the age of 12 months became significantly lower than that in wild type mice (Fig. 7).

7. Progressive neuroinflammation in *Hgsnat-Geo* mice

Chronic progressive neuroinflammation is well documented in mouse models of lysosomal neurodegenerative diseases including those of MPS IIIA and B, which are characterized by activation of resident microglia and astrocytes, infiltration of leucocytes from the periphery and production of the inflammatory cytokines(Ausseil *et al.*, 2008; Ohmi *et al.*, 2003; Wilkinson *et al.*, 2012). Two fold increased expression of inflammation markers, MIP1α (CCL3) and TNFα, in the brains of homozygous *Hgsnat-Geo* mice was detected as early as at 10 days after birth. The levels of these cytokines further increased with age reaching the maximum at 8 months of age (Fig. 8A). At the same time, IL-1-β and TGF-β were not significantly increased as compared with wild type controls. Similarly increased expression of MIP1α and TNFα cytokines was detected also in the brain tissues of MPS IIIA mice, whereas MPS IIIB mice had ~2 fold higher levels at all ages.

Consistent with high expression level of cytokines brain tissues of Hgsnat-deficient mice showed increased levels of activated microglia cells detected by isolectin B4 staining (Fig. 8B) or

antibodies against CD68 (Fig. 3B), whereas almost no staining was detected in matching controls. Besides, significantly higher amount of astrocytes stained with anti-GFAP antibodies was detected in the hippocampal area of mutant mice starting from the age of 4 months (Fig. 3B).

Signs consistent with an immune reaction were detected also in the liver. Early activation of Kupffer cells preceding the substantial storage and increased presence in liver sinusoids of inflammatory cells was detectable in *Hgsnat-Geo* mice but not in wild type mice (Fig. S4).

Discussion

Altogether our data demonstrate that HGSNAT deficiency in mice results in lysosomal accumulation of HS, in multiple cell types, including brain neurons and microglia. In brain neurons HS accumulation is accompanied by secondary accumulation of gangliosides and increased lysozyme, pTau, Gsk3β, and beta amyloid levels. Signs of general inflammation in the brain including activation of astrocytes, microglia and cytokine production, previously reported for other MPS mouse models are clearly present from the very early age. At the same time a lower level of GAG storage as compared to the MPS IIIB mouse model results in a reduced level of brain inflammation, later onset and slower progression of the disease.

The main organs affected at the optical and ultrastructural levels are the brain, liver and spleen. Lysosomal storage consistent with accumulation of undegraded GAG developed early in hepatocytes, splenic sinus endothelium, and cerebral microglia, and to a lesser extent in liver Kupffer and Ito cells, in fibroblasts and in perivascular cells. In peripheral tissues, storage in epithelial and mesenchymal cells, except for hepatocytes occurred later and with a lesser intensity as compared to mouse MPS IIIA and MPS IIIB models(Bhaumik *et al.*, 1999; Li *et al.*, 1999). Presence of macrophages with storage materials in visceral organs was limited, except for liver Kupffer cells, which were activated and developed storage phenotype with age.

In the brain, substantial HS storage in microglia was found as early as at 2 months and seems to be the initial pathological event more evident at the age of 2-4 months then pathological changes in neurons, and possibly explained by high phagocytic activity of microglia causing an extracellular substrate burden. The storage was further increased with age in all examined brain regions. Foam microglial cells were frequently in a close contact to neurons. Storage vacuoles in microglia had a uniform electron-lucent appearance different from ceroid-type accumulation in neurons. The apparently different storage patterns detected in microglia and neurons by EM could be also attributed to the loss of GAG during fixation of the cells, however further immunohistochemical analysis confirmed that lysosomal storage of HS in microglia exceeded that in neurons, whereas gangliosides accumulated mainly in neurons.

Neuronal pathology was also featured by cytoplasmic accumulation of densely packed material in neuronal perikarya, which was likely a source of strong autofluorescence and positive immunostaining for SCMAS. Storage of granular autofluorescent material restricted to individual neurons at 5 months was detected throughout the whole neuronal population at 12 months, but even at this advanced stage, neurons showed variations in the amount of stored materials between brain regions and between cells within a region. Similar heterogeneous storage character was reported for the other MPS disease mouse models (McGlynn *et al.*, 2004). Neuronal loss was not a dominant feature at the early stage of the disease but it became significant at 10 months and further progressed with age. At the EM level, neuronal pathology was characterized by a combination of early detectable structural alterations in mitochondria, progressive lysosomal storage of heterogeneous material and massive lysosomal accumulation of deposits resembling those detected in neuronal ceroid lipofuscinoses. Similar “fingerprint-like” structures were previously detected in MPS IIIB mouse and identified as SCMAS aggregates (Ryazantsev *et al.*, 2007). The mitochondrial network in neurons was disorganized and the partial impairment of OXPHOS enzymes (complex II, II+III and IV) in brain

tissues was detected by enzymatic assays and immunohistochemical analysis, while mitochondrial compartment in age-matching controls did not reveal any abnormalities.

Altogether our data characterize MPS IIIC as a neurodegenerative disorder with a dominant lysosomal and mitochondrial alterations in neurons. Furthermore, our findings suggest that autophagy, namely mitophagy represents a substantial source for accumulation of undegraded materials in the lysosomal system of neurons.

The precise sequence of events that starts with the accumulation of HS and leads to a widespread brain pathology and neuronal death is yet to be determined, however our results allow hypothesizing that the malfunction and loss of neurons can be at least partially mediated by pathological changes in their mitochondrial system. We speculate that the disease starts with accumulation of primary storage materials (mostly HS and HS-derived oligosaccharides) as documented by EM analysis and immunohistochemistry with HS-specific antibodies. These materials released presumably by exocytosis of lysosomes are known to induce general inflammation reactions in the brain by activating TLR receptors of microglia cells, resulting in release of multifunctional cytokines such as TNF-α and MIP-1-α, known to cause mitochondrial damage through formation of ROS and oxidative stress(Baregamian *et al.*, 2009; Chen *et al.*, 2010; Chuang *et al.*, 2012; Vitner *et al.*, 2012) eventually leading to neuronal death observed in somatosensory cortex and cerebellum (Purkinje cells). In the cerebellar cortex, Purkinje cells degeneration typically observed in other LSDs (Macauley *et al.*, 2008; Sarna *et al.*, 2001) was also present. Although neurodegenerative disease can develop even without neuronal loss it is important to mention that neuronal death is observed in MPS III patients(Hamano *et al.*, 2008). Ganglioside accumulation detected in neurons starting from 2 months is probably of non-lysosomal origin. It could be caused by altered Golgi function as described previously for MPS IIIB mouse model(Roy *et al.*, 2012). Stored lipids and gangliosides can also be partially of mitochondrial origin due to mitophagy and impaired catabolism of autophagosomal

content. Indeed, our data define accumulation of densely packed material displaying a strong autofluorescence as a determining feature in brain neurons of MPS IIIC mice at the advanced stage of the disease. Since these granules are SCMAS positive and their ultrastructural pattern strongly resembles that in neuronal ceroid lipofuscinoses we speculate that they are derived from autophagosomes. Impairment of autophagosome-lysosome fusion can also result in accumulation of deformed and misfunctional mitochondria otherwise eliminated through autophagy and lysosomal catabolism (de Pablo-Latorre *et al.*, 2012; Osellame *et al.*, 2013). Out data suggest that autophagic alterations may be involved in the neuropathological changes in *Hgsnat-Geo* mouse nevertheless it remains to be determined whether autophagy is impaired or in contrast increased since the detected LC3-II accumulation can reflect both increased autophagy or defective proteolysis following formation of the autophagosome.

Together, our data validate *Hgsnat-Geo* mouse as an animal model relatively well matching phenotype of human MPS IIIC. MPS IIIC stands out among lysosomal diseases since it is the only one caused by a deficiency of not a hydrolase but a transferase. It is also one of rare disorders involving defects of an integral membrane protein untreatable by enzyme replacement or hematopoietic stem cell therapy. This makes *Hgsnat-Geo* mouse a valuable model for experimental evaluation of the efficacy of novel therapeutic strategies that can be potentially applied for such disorders, including gene therapy, substrate deprivation therapy or novel methods of enzyme delivery. Besides, our model can provide important opportunity to better understand underlying pathogenic mechanisms of the disease, particularly regarding the central nervous system, given that human material is highly limited due to the relative rarity of MPS IIIC. Finally, the mechanism of brain disease in MPS IIIC mouse model involving mitochondrial dysfunction and brain inflammation may represent a common phenomenon for metabolic neurodegenerative diseases. It also justifies future studies to determine if

the mitochondrial defects in MPS IIIC cells can be at least partially rescued by known anti-oxidative drugs.

Acknowledgements

Authors acknowledge Drs. Elizabeth Neufeld, Jakub Sikora and Mila Ashmarina for critical reading of the manuscript and helpful advice. We also thank Dr. Nobuo Hanai, Dr. Akiko Furuya and Kyowa Hakko Kirin Co., Ltd. for a generous gift of monoclonal antibodies against G_{M2} ganglioside, Dr. Pascal Vachon for the help with neurological examination of mice, Saadallah Bouhanik for the help with X-ray analysis, Dr. Volkan Seyrantepe for the help with ganglioside analysis by TLC and Carmen Movila for the help in preparation of the manuscript.

This work was supported in part by the operating grant (111068) from Canadian Institutes of Health Research and from JJB Foundation to A.V.P., the grant NT13122-3/2012 from the Ministry of Health of the Czech Republic to Helena Hůlková and M.H. and by Charles University institutional program PRVOUK-P24/LF1/3 to Hana Hansíková, M.T. and Z.H. C.M. acknowledges the Ph.D. scholarship from the Portuguese Foundation for Science and Technology (FCT).

References

Aronovich, E.L., et al., 2000. Canine heparan sulfate sulfamidase and the molecular pathology underlying Sanfilippo syndrome type A in Dachshunds. Genomics. 68**,** 80-4.

Aronovich, E.L., et al., 2001. Molecular basis of mucopolysaccharidosis type IIIB in emu (Dromaius novaehollandiae): an avian model of Sanfilippo syndrome type B. Genomics. 74**,** 299-305.

Ausseil, J., et al., 2008. Early neurodegeneration progresses independently of microglial activation by heparan sulfate in the brain of mucopolysaccharidosis IIIB mice. PLoS One. 3**,** e2296.

Baregamian, N., et al., 2009. Tumor necrosis factor-alpha and apoptosis signal-regulating kinase 1 control reactive oxygen species release, mitochondrial autophagy, and c-Jun N-terminal kinase/p38 phosphorylation during necrotizing enterocolitis. Oxid Med Cell Longev. 2**,** 297-306.

Bartsocas, C., et al., 1979. Sanfilippo type C disease: clinical findings in four patients with a new variant of mucopolysaccharidosis III. Eur J Pediatr. 130**,** 251-8.

Bhaumik, M., et al., 1999. A mouse model for mucopolysaccharidosis type III A (Sanfilippo syndrome). Glycobiology. 9**,** 1389-96.

Bifsha, P., et al., 2007. Altered gene expression in cells from patients with lysosomal storage disorders suggests impairment of the ubiquitin pathway. Cell Death Differ. 14**,** 511-23.

Chatham, J.C., Marchase, R.B., 2010. Protein O-GlcNAcylation: A critical regulator of the cellular response to stress. Curr Signal Transduct Ther. 5**,** 49-59.

Chen, X.H., et al., 2010. TNF-alpha induces mitochondrial dysfunction in 3T3-L1 adipocytes. Mol Cell Endocrinol. 328**,** 63-9.

Chuang, Y.C., et al., 2012. Macrophage migration inhibitory factor induces autophagy via reactive oxygen species generation. PLoS One. 7**,** e37613.

Crawley, A.C., et al., 2006. Characterization of a C57BL/6 congenic mouse strain of mucopolysaccharidosis type IIIA. Brain Res. 1104**,** 1-17.

David, G., et al., 1992. Developmental changes in heparan sulfate expression: in situ detection with mAbs. J Cell Biol. 119**,** 961-75.

de Pablo-Latorre, R., et al., 2012. Impaired parkin-mediated mitochondrial targeting to autophagosomes differentially contributes to tissue pathology in lysosomal storage diseases. Hum Mol Genet. 21**,** 1770-81.

de Ruijter, J., et al., 2013. High prevalence of femoral head necrosis in Mucopolysaccharidosis type III (Sanfilippo disease): a national, observational, cross-sectional study. Mol Genet Metab. 109**,** 49-53.

DiRosario, J., et al., 2009. Innate and adaptive immune activation in the brain of MPS IIIB mouse model. J Neurosci Res. 87**,** 978-90.

Dudkova, Z., et al., 1995. Determination of pyruvate dehydrogenase Complex Activity in Muscle Tissue. Klin. Biochem. Metab. 3**,** 178-182.

Durand, S., et al., 2010. Analysis of the biogenesis of heparan sulfate acetyl-CoA:alpha-glucosaminide N-acetyltransferase provides insights into the mechanism underlying its complete deficiency in mucopolysaccharidosis IIIC. J Biol Chem. 285**,** 31233-42.

Ellinwood, N.M., et al., 2003. A model of mucopolysaccharidosis IIIB (Sanfilippo syndrome type IIIB): N-acetyl-alpha-D-glucosaminidase deficiency in Schipperke dogs. J Inherit Metab Dis. 26**,** 489-504.

Feldhammer, M., Durand, S., Pshezhetsky, A.V., 2009. Protein misfolding as an underlying molecular defect in mucopolysaccharidosis III type C. PLoS One. 4**,** e7434.

Ginsberg, S.D., et al., 1999. Accumulation of intracellular amyloid-beta peptide (A beta 1-40) in mucopolysaccharidosis brains. J Neuropathol Exp Neurol. 58**,** 815-24.

Hamano, K., et al., 2008. Mechanisms of neurodegeneration in mucopolysaccharidoses II and IIIB: analysis of human brain tissue. Acta Neuropathol. 115**,** 547-59.

Hansen, G.M., et al., 2008. Large-scale gene trapping in C57BL/6N mouse embryonic stem cells. Genome Res. 18**,** 1670-9.

Hocquemiller, M., et al., 2010. GAP43 overexpression and enhanced neurite outgrowth in mucopolysaccharidosis type IIIB cortical neuron cultures. J Neurosci Res. 88**,** 202-13.

Huang, J.Q., et al., 1997. Apoptotic cell death in mouse models of GM2 gangliosidosis and observations on human Tay-Sachs and Sandhoff diseases. Hum Mol Genet. 6**,** 1879-85.

Klein, U., Kresse, H., von Figura, K., 1978. Sanfilippo syndrome type C: deficiency of acetyl-CoA:alpha-glucosaminide N-acetyltransferase in skin fibroblasts. Proc Natl Acad Sci U S A. 75**,** 5185-9.

Kyrklund, T., 1987. Two procedures to remove polar contaminants from a crude brain lipid extract by using prepacked reversed-phase columns. Lipids. 22**,** 274-7.

Langford-Smith, A., et al., 2011a. Female mucopolysaccharidosis IIIA mice exhibit hyperactivity and a reduced sense of danger in the open field test. PLoS One. 6**,** e25717.

Langford-Smith, A., et al., 2011b. Hyperactive behaviour in the mouse model of mucopolysaccharidosis IIIB in the open field and home cage environments. Genes Brain Behav. 10**,** 673-82.

Lema, P.P., Girard, C., Vachon, P., 2004. Evaluation of dexamethasone for the treatment of intracerebral hemorrhage using a collagenase-induced intracerebral hematoma model in rats. J Vet Pharmacol Ther. 27**,** 321-8.

Li, H.H., et al., 1999. Mouse model of Sanfilippo syndrome type B produced by targeted disruption of the gene encoding alpha-N-acetylglucosaminidase. Proc Natl Acad Sci U S A. 96**,** 14505-10.

Lowry, O.H., et al., 1951. Protein measurement with the Folin phenol reagent. J Biol Chem. 193**,** 265-75.

Macauley, S.L., et al., 2008. Neuropathology of the acid sphingomyelinase knockout mouse model of Niemann-Pick A disease including structure-function studies associated with cerebellar Purkinje cell degeneration. Exp Neurol. 214**,** 181-92.

Makinen, M.W., Lee, C.P., 1968. Biochemical studies of skeletal muscle mitochondria. I. Microanalysis of cytochrome content, oxidative and phosphorylative activities of mammalian skeletal muscle mitochondria. Arch Biochem Biophys. 126**,** 75-82.

McGlynn, R., Dobrenis, K., Walkley, S.U., 2004. Differential subcellular localization of cholesterol, gangliosides, and glycosaminoglycans in murine models of mucopolysaccharide storage disorders. J Comp Neurol. 480**,** 415-26.

Mohammed, E.E., et al., 2012. Accelerated clinical disease and pathology in mucopolysaccharidosis type IIIB and GalNAc transferase double knockout mice. Mol Genet Metab. 107**,** 129-35.

Mosca, F., et al., 2002. Assay of coenzyme Q(10) in plasma by a single dilution step. Anal Biochem. 305**,** 49-54.

Nakamura, K., et al., 1994. Chimeric anti-ganglioside GM2 antibody with antitumor activity. Cancer Res. 54**,** 1511-6.

Neufeld, E.F., Muenzer, J., 2001. The Mucopolysaccharidoses. In: The Metabolic and Molecular Basis of Inherited Disease. Vol., C.R. Scriver, A.L. Beaudet, W.S. Sly, D. Valle, eds. McGraw-Hill, USA, New-York, pp. 3421-3452.

Ohmi, K., et al., 2003. Activated microglia in cortex of mouse models of mucopolysaccharidoses I and IIIB. Proc Natl Acad Sci U S A. 100**,** 1902-7.

Ohmi, K., et al., 2009. Sanfilippo syndrome type B, a lysosomal storage disease, is also a tauopathy. Proc Natl Acad Sci U S A. 106**,** 8332-7.

Ohmi, K., Zhao, H.Z., Neufeld, E.F., 2011. Defects in the medial entorhinal cortex and dentate gyrus in the mouse model of Sanfilippo syndrome type B. PLoS One. 6**,** e27461.

Osellame, L.D., et al., 2013. Mitochondria and quality control defects in a mouse model of Gaucher disease--links to Parkinson's disease. Cell Metab. 17**,** 941-53.

Pinto, R., et al., 2004. Prevalence of lysosomal storage diseases in Portugal. Eur J Hum Genet. 12**,** 87-92.

Poorthuis, B.J., et al., 1999. The frequency of lysosomal storage diseases in The Netherlands. Hum Genet. 105**,** 151-6.

Roy, E., et al., 2012. GM130 gain-of-function induces cell pathology in a model of lysosomal storage disease. Hum Mol Genet. 21**,** 1481-95.

Ruijter, G.J., et al., 2008. Clinical and genetic spectrum of Sanfilippo type C (MPS IIIC) disease in The Netherlands. Mol Genet Metab. 93**,** 104-11.

Rustin, P., et al., 1994. Biochemical and molecular investigations in respiratory chain deficiencies. Clin Chim Acta. 228**,** 35-51.

Ryazantsev, S., et al., 2007. Lysosomal accumulation of SCMAS (subunit c of mitochondrial ATP synthase) in neurons of the mouse model of mucopolysaccharidosis III B. Mol Genet Metab. 90**,** 393-401.

Sarna, J., et al., 2001. Patterned cerebellar Purkinje cell death in a transgenic mouse model of Niemann Pick type A/B disease. Eur J Neurosci. 13**,** 1873-80.

Settembre, C., et al., 2013. Signals from the lysosome: a control centre for cellular clearance and energy metabolism. Nat Rev Mol Cell Biol. 14**,** 283-96.

Seyrantepe, V., et al., 2008. Mice deficient in Neu4 sialidase exhibit abnormal ganglioside catabolism and lysosomal storage. Hum Mol Genet. 17**,** 1556-68.

Seyrantepe, V., et al., 2010. Mice doubly-deficient in lysosomal hexosaminidase A and neuraminidase 4 show epileptic crises and rapid neuronal loss. PLoS Genet. 6.

Srere, P.A., 1969. [1] Citrate synthase: [EC 4.1.3.7. Citrate oxaloacetate-lyase (CoA-acetylating)]. In: Methods Enzymol. Vol. Volume 13, M.L. John, ed.^eds. Academic Press, pp. 3-11.

Valstar, M.J., et al., 2008. Sanfilippo syndrome: a mini-review. J Inherit Metab Dis. 31**,** 240-52.

Villani, G.R., et al., 2007. Cytokines, neurotrophins, and oxidative stress in brain disease from mucopolysaccharidosis IIIB. J Neurosci Res. 85**,** 612-22.

Vitner, E.B., et al., 2012. Contribution of brain inflammation to neuronal cell death in neuronopathic forms of Gaucher's disease. Brain. 135**,** 1724-35.

Wada, R., Tifft, C.J., Proia, R.L., 2000. Microglial activation precedes acute neurodegeneration in Sandhoff disease and is suppressed by bone marrow transplantation. Proc Natl Acad Sci U S A. 97**,** 10954-9.

Whitley, C.B., et al., 1989. Diagnostic test for mucopolysaccharidosis. I. Direct method for quantifying excessive urinary glycosaminoglycan excretion. Clin Chem. 35**,** 374-9.

Wilkinson, F.L., et al., 2012. Neuropathology in mouse models of mucopolysaccharidosis type I, IIIA and IIIB. PLoS One. 7**,** e35787.

Zambrowicz, B.P., et al., 2003. Wnk1 kinase deficiency lowers blood pressure in mice: a gene-trap screen to identify potential targets for therapeutic intervention. Proc Natl Acad Sci U S A. 100**,** 14109-14.

Figure Legends

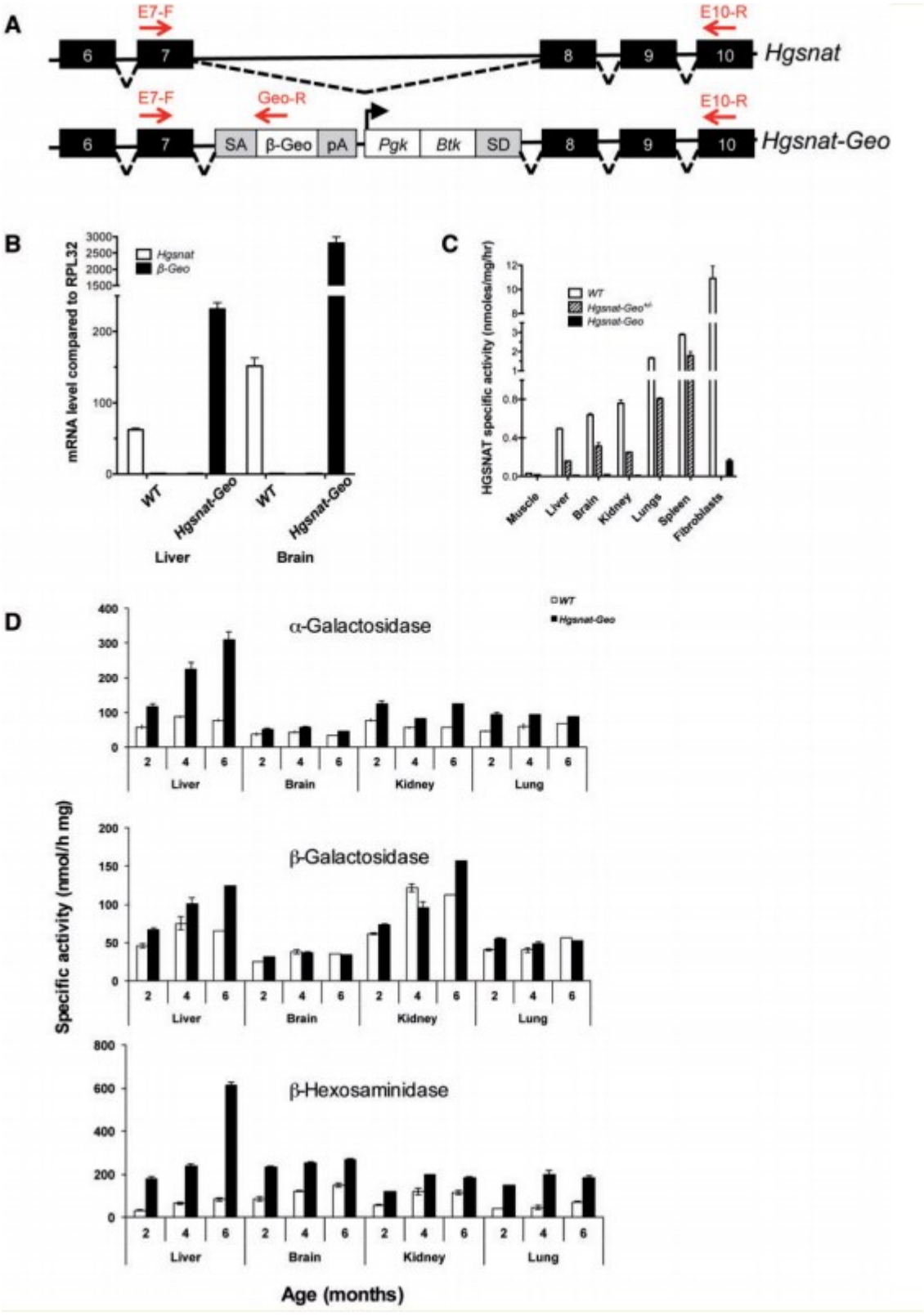

Figure 1. Targeting the *Hgsnat* gene in mice.

(A) Strategy for producing the targeted disruption of the *Hgsnat* gene. The gene trap vector used by TIGM contains a splice acceptor site (SA) upstream of a β-galactosidase/neomycin phosphotransferase (*Geo*) fusion gene followed by polyadenylation sequence (pA), *PGK* and *BTK* genes and splice donor site (SD) inserted into intron 7 of the *Hgsnat* gene as confirmed by genomic sequencing. Hence, the downstream exons 8–13 in the gene trap transcript were replaced by the Geo sequence. Exons in the mouse *Hgsnat* gene are shown as black numbered boxes and *Geo-PGK-BTK* cassette, as white boxes. Primers (E7-R, Geo-R, and E10-F) were used to measure the expression of the wild type *Hgsnat* and of the targeted *Hgsnat-Geo* alleles by RT-qPCR.

(B) RT-qPCR shows that expression of the *Hgsnat* mRNA in brain and liver tissues of mice homozygous for the *Hgsnat-Geo* allele is reduced to 0.6 and 1.6% of that in the tissues of their wild type siblings. Total RNA was extracted from tissues of 4-month-old wild type and *Hgsnat-Geo* mice and analyzed for *Hgsnat* expression by RT-qPCR. The values were normalized for the level of control *RPL32* mRNA. Data are expressed as means (±S.D.) of experiments performed with 6 mice for each genotype.

(C) Deficient Hgsnat activity in tissues of mice homozygous for *Hgsnat-Geo* allele. Hgsnat activity was measured with fluorogenic substrate, Muf-β-D-glucosaminide in the tissues of 4-month-old wild type, *Hgsnat-Geo*$^{+/-}$ and *Hgsnat-Geo* mice or in cultured skin fibroblasts of wild type and *Hgsnat-Geo* mice. Data are expressed as means (±S.D.) of independent experiments performed with tissues of six mice for each genotype or with three different cell cultures.

(D) Lysosomal hydrolases are increased in tissues of *Hgsnat-Geo* mice. Acidic α-galactosidase, β-galactosidase and total β-hexosaminidase activity were measured in the tissues of 1, 4 and 6 month-old *Hgsnat-Geo* mice and their wild type siblings. Data are expressed as means (±S.D.) of experiments performed with three mice for each genotype.

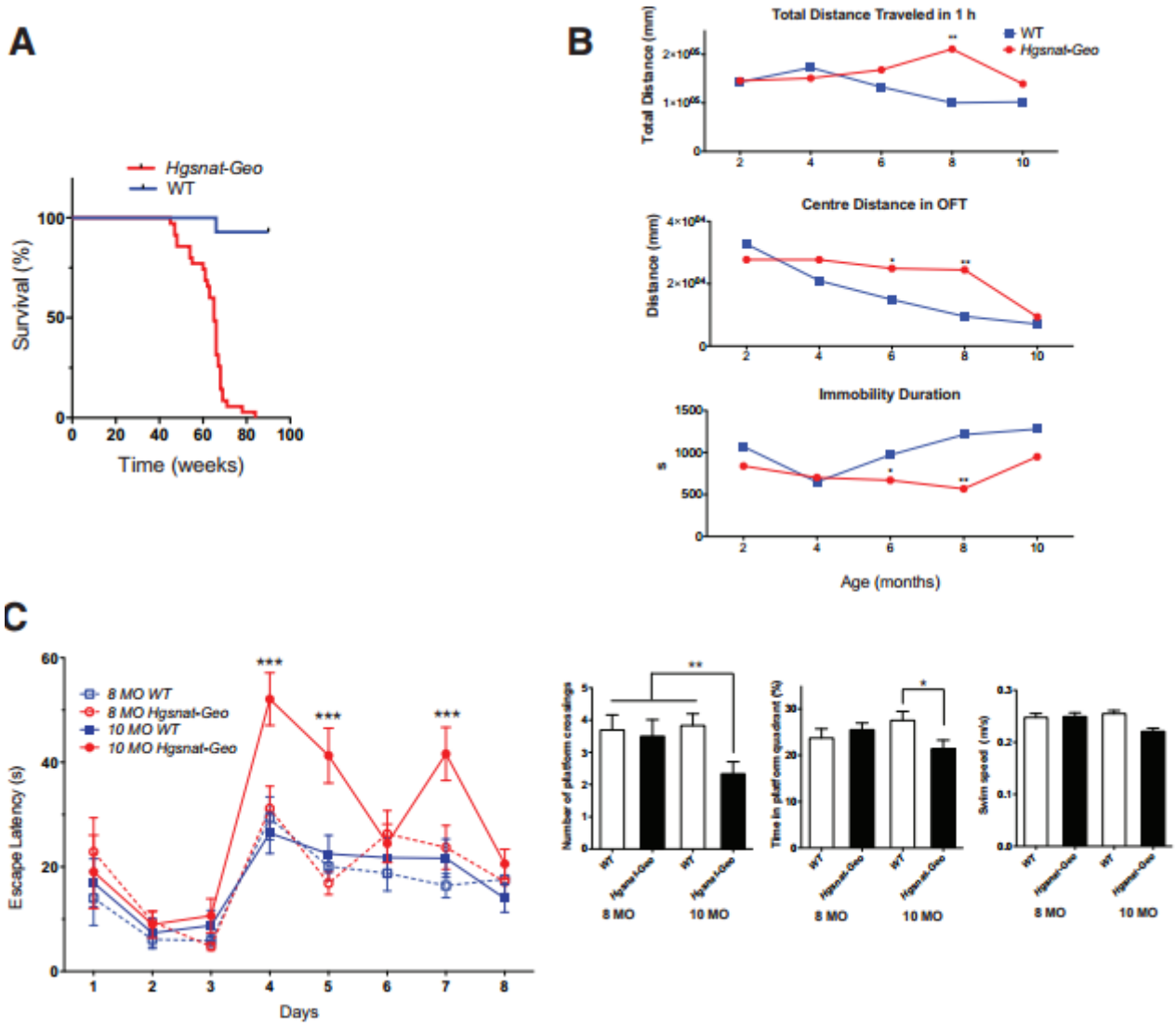

Figure 2. *Hgsnat-Geo* mice have shorter life span and show signs of hyperactivity between the ages of 6 and 8 months and learning impairment at the age of 10 months.

(A) Kaplan-Meier plot showing survival of *Hgsnat-Geo* mice ($n = 50$) and their wild type counterparts ($n = 70$). By the age of 70 weeks the vast majority of *Hgsnat-Geo* mice died or had to be euthanized on the veterinarian request due to urinary retention.

(B) Six and 8-month-old *Hgsnat-Geo* female mice show signs of hyperactivity and reduced anxiety compared to wild type mice as detected by open field test performed 1 h into their light cycle. Increased activity (total distance traveled) was detected starting from ~5 months of age, with significant hyperactivity at 8 months. Reduced anxiety (increased center activity) was detected starting from ~3

months, with significant difference with wild type at 6 and 8 months. At 6 and 8 months *Hgsnat-Geo* mice also spent significantly less time immobile as compared to wild type mice. P value was calculated by two-way-ANOVA (* $P < 0.05$, ** $P < 0.01$). From 6 (2, 4 and 6 month old) to 10 (8 and 10 month old) naive mice were studied per age/per genotype.

(C) *Hgsnat-Geo* mice showed impaired performance in the spatial memory-based Morris Water Maze test at 10 months. All mice showed similar average latencies on days 1-3 of visible platform testing. Whereas 8-month-old *Hgsnat-Geo* mice had latencies in the hidden platform testing similar to those of their wild type counterparts (days 4-8), 10-month-old mutant mice were significantly impaired in this spatial learning test. During the removed-platform probe trial on day 9, *Hgsnat-Geo* mice displayed reduced time in the target quadrant as compared to their wild type siblings. Numbers of passes over the previous location of the hidden platform were also reduced. Swim speed was comparable among all groups. Six mice were studied for each group. P value for escape latency was calculated by two-way-ANOVA (*** $P < 0.001$) and for the number of platform crossing and time in platform quadrant, by t-test (* $P < 0.05$, ** $P < 0.01$).

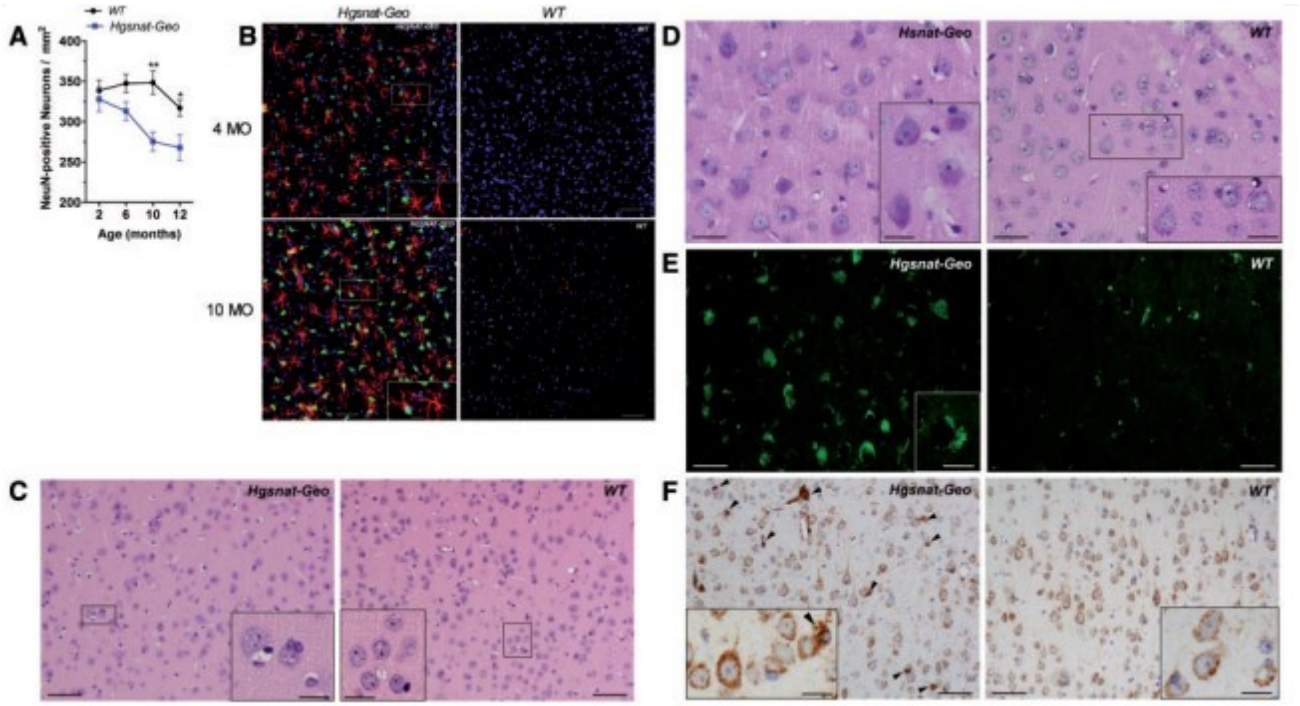

Figure 3. Pathological changes in CNS of *Hgsnat-Geo* mice

(A) Progressive loss of neurons in somatosensory cortex. NeuN-positive neurons were counted by two observers blinded for the mouse genotype in two similar fields on 3 sagittal sections (cut 1.44, 1.68 and 1.92 mm from bregma) of S1 somatosensory cortex of each mouse; four (two male, two female) mice were studied for each age and each genotype. Two-way (age and genotype) ANOVA was used to test differences between the mouse groups: significant differences between the genotypes at a given age in Bonferroni post-test (* $P < 0.05$, ** $P < 0.01$) are shown.

(B) Increased numbers of GFAP-positive astrocytes and C68-positive microglia are detected in the somatosensory cortex of *Hgsnat-Geo* mice. Somatosensory cortex (layer V) of 4-month and 10-month-old *Hgsnat-Geo* mouse and wild type littermate control (*WT*); slides stained with chicken polyclonal antibodies against GFAP (AbCam ab4674, 1/600) and rat antibodies against mouse CD68 (MCA 1957, 1/400), followed by Dylight TM 549-conjugated goat anti-chicken IgG (Jackson ImmunoResearch Laboratories 103-505-155, 1/50) and Alexa fluor 488-conjugated goat anti-rat IgG (Invitrogen, 1/400)

antibodies. The nuclei were stained with DRAQ5 TM, (Thermo Scientific 62254, 1/ 1000). Bars represent 50 μm, bars in the inserts, 20 μm.

(C) Presence in cortical gray matter of microglial cells with vacuolized cytoplasm and foam-like appearance. Microglial cells showing storage are either dispersed or adjacent to neurons (shown in details in the insert). Somatosensory cortex (layer V) of 12-month-old *Hgsnat-Geo* mouse and wild type littermate control (*WT*); H&E stain. Bars represent 100 μm, bars in the inserts, 30 μm.

(D) Accumulation of PAS positive granular material is detectable in perikarya of multiple neurons in the brain of *Hgsnat-Geo* mouse. Microglia show presence of storage and foam-like appearance. Brain of wild type littermate control displays only discrete PAS positive deposits corresponding with age pigment. Inserts show detailed views of neurons and microglia. Somatosensory cortex (layer V) of 12-month-old *Hgsnat-Geo* and wild type mice. Bars represent 50 μm, bars in the inserts, 30 μm.

(E) A massive accumulation of granular autofluorescent ceroid is widely present in cortical neurons of 12-month-old *Hgsnat-Geo* mouse. Insert shows a detailed view of a neuron with ceroid deposits in the perikaryon. Brain of wild type littermate control contains a small amount of autofluorescent lipofuscin in individual neurons. Somatosensory cortex (layer V) of 12-month-old *Hgsnat-Geo* mouse. Bars represent 100 μm, bar in the insert, 30 μm.

(F) Increased cathepsin D immunostaining comparable with lysosomal storage in microglia and neurons of 12-month-old *Hgsnat-Geo* mouse. Dispersed, perineuronal or perivascular microglia is strongly positive for Cathepsin D (marked by arrowheads). Lysosomal system in neurons is irregularly activated and shows a coarsely granular appearance. Neuronal perikarya are not markedly distended in contrast to microglia. Inserts show detailed views of both cell types. Somatosensory cortex (layer V) of 12-month-old *Hgsnat-Geo* and wild type mice. Bars represent 100 μm, bars in the inserts, 30 μm.

Panels show representative images of at least 30 studied for 4 *Hgsnat-Geo* and 4 wild type mice.

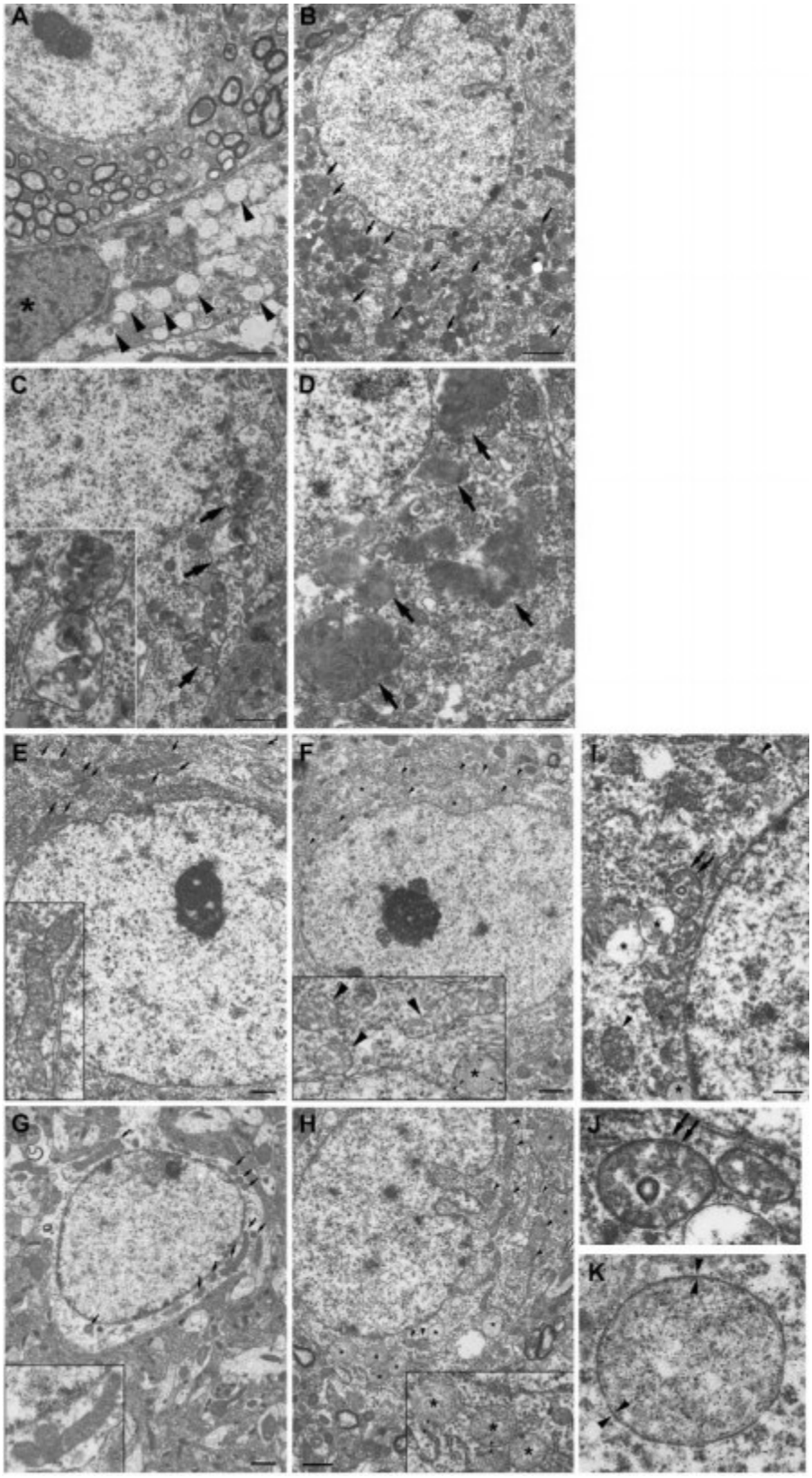

Figure 4. Ultrastructural pathology in the brain of *Hgsnat-Geo* mice.

(A) Storage pattern in microglia detected at 5 months. Massive accumulation of vacuoles with single limiting membranes and a sparse fine content in the cytoplasm of a cortical microglial cell is compatible with lysosomal GAG storage. Lysosomes containing storage materials are marked by arrowheads. The microglial cell (nucleus is marked by an asterisk) is in a close proximity to a cortical brain neuron. Bar represents 2 μm.

(B) Lysosomal system in a cortical neuron at 12 months is expanded and massively overloaded by electron dense material (marked by arrows). Bar represents 2 μm.

(C) High magnification micrograph of a cortical neuron at 12 moths demonstrates a storage compartment (marked by arrows) containing ceroid-like granular and/or lamellar material packed with a variable density as well as occasional lipid droplets. Insert shows a detailed view of storage deposits. Bar represents 1 μm.

(D) Storage of densely packed fibrillary material (marked by arrows) strongly resembling rectilinear or fingerprint-like ceroid deposits in neuronal lysosomes at advanced stages of the disease. Brain cortex of 16-month-old *Hgsnat-Geo* mouse. Bar represents 1 μm.

Mitochondrial population in neurons of wild type mice at the age of 5 **(E)** and 12 months **(G)** is relatively uniform and is composed of normally shaped mitochondria (marked by arrows) with largely regular cristae (details are shown in the inserts). Bar represents 1 μm.

Mitochondria in a neuron of *Hgsnat-Geo* mouse at the age of 5 months **(F)** are relatively numerous and pleiomorphic with some of them revealing incipient swelling (marked by arrowheads). Edematous mitochondria with largely dissolved cristae (marked by asterisks) but with remnants of double membranes (marked by double arrowheads) were detected occasionally. A detailed view of incipient mitochondrial abnormalities is shown in the insert. Bar represents 1 μm.

At the age of 12 months **(H)**, mitochondria in neurons of *Hgsnat-Geo* mice are clearly pleiomorphic with many of them displaying swelling and disorganization of their inner membranes (marked by

arrowheads). Substantially edematous mitochondria with largely dissolved cristae are marked by asterisks. Insert shows a detailed view of highly edematous mitochondria with remnants of double membranes (marked by double arrowheads). Bar represents 1μm.

(I) A higher magnification demonstrates structural mitochondrial abnormalities in a neuron of *Hgsnat-Geo* mouse at 12 months. Mitochondria are swollen with disorganized (arrowheads) or even dissolved (asterisks) cristae and occasionally contain circular formations (marked by double arrows). Bar represents 500 nm.

(J) A detailed view of a mitochondrion with inner membranes forming circular structures.

(K) A detailed view of a highly edematous mitochondrion with dissolved cristae but with detectable remnants of double membranes (marked by double arrowheads).

Panels show representative images of at least 30 studied for 3 *Hgsnat-Geo* and 3 wild type mice for each age.

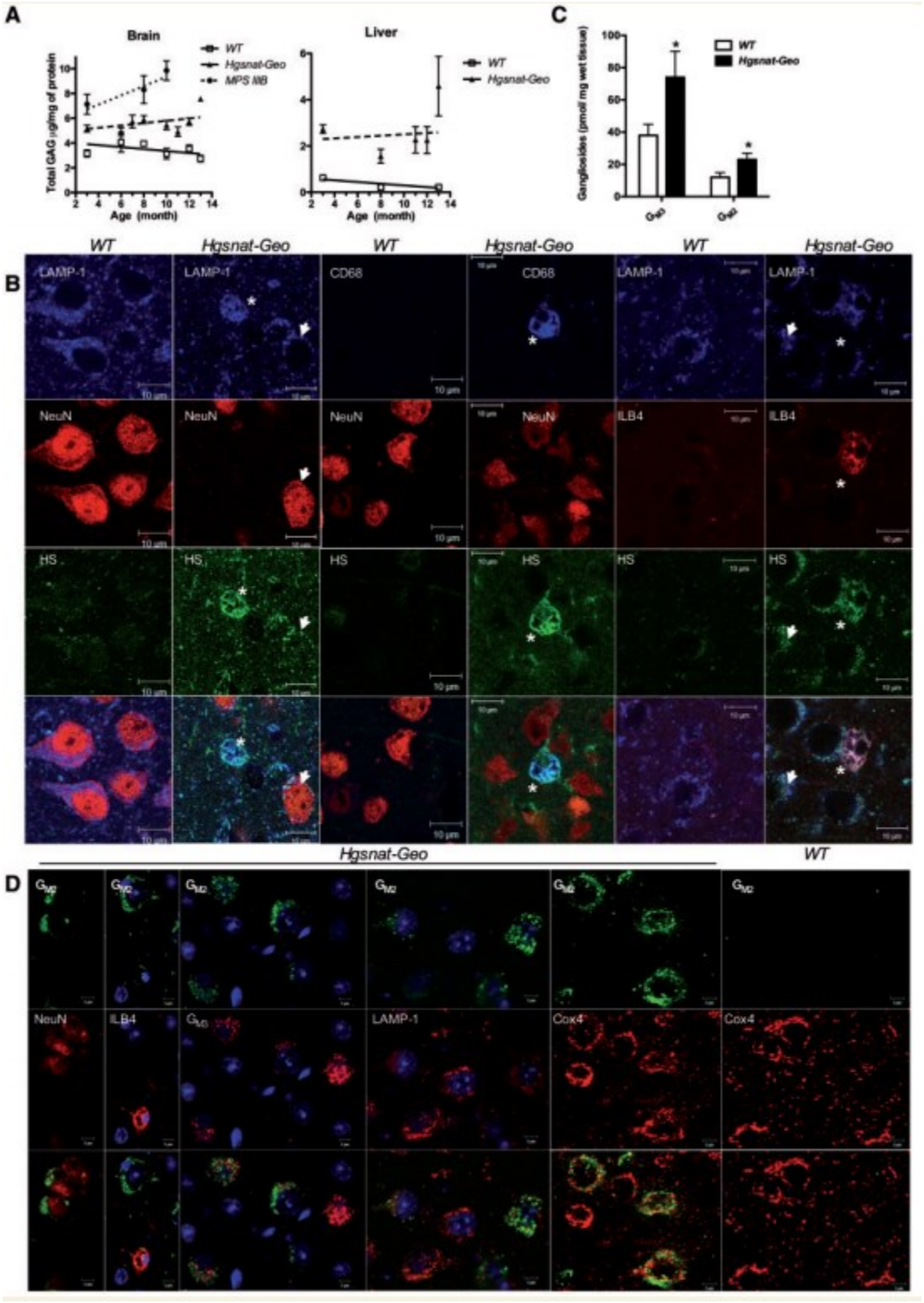

Figure 5. Accumulation of primary and secondary storage materials in tissues of *Hgsnat-Geo* mice

A) Total GAG were measured in the whole brain tissues of *Hgsnat-Geo* mice, α-N-acetylglucosaminidase-deficient (MPS IIIB) mice and their corresponding wild type controls as well as in liver tissues of *Hgsnat-Geo* and wild type mice. The data show means (±S.D.) of individual measurements performed with 15 mice for each age and genotype.

B) Intralysosomal accumulation of heparan sulfate in the brain cells of *Hgsnat-Geo* mice. Forty μm-thick sagittal brain sections of 4-month-old wild type and *Hgsnat-Geo* mice were stained with anti-HS and anti-LAMP-1 antibodies and either antibody against neuronal marker NeuN or microglial marker, isolectin B4 (ILB4) or with antibodies against HS, NeuN and CD68. Somatosensory cortex of wild type mouse does not show HS (green) staining while that of *Hgsnat-Geo* mouse contains multiple neurons (arrowheads) or microglia (asterisks) with lysosomal accumulation of HS. Foamy microglia (negative for neuronal marker, NeuN, but positive for ILB4 or CD68) show on average an increased staining for HS compared to neurons.

C) Levels of G_{M3} and G_{M2} gangliosides are increased in the total brain extracts of 4-month-old *Hgsnat-Geo* mice as compared to their wild type siblings. Total lipids from brain tissue homogenates were extracted with chloroform/methanol 1:1 mixture and analyzed by tandem mass spectroscopy.

D) Accumulation of gangliosides in cortical neurons of *Hgsnat-Geo* mice. Forty μm-thick sagittal brain sections of 8-month-old wild type and *Hgsnat-Geo* mice were stained with anti-G_{M2} antibodies and either microglial marker, isolectin B4 or antibodies against neuronal marker NeuN, G_{M3} ganglioside, LAMP-1 and mitochondrial marker, cytochrome c oxidase subunit 4 (Cox4). Slides were studied on a Zeiss LSM510 inverted confocal microscope.

Panels show representative images of at least 30 studied for 3 *Hgsnat-Geo* and 3 wild type mice for each age.

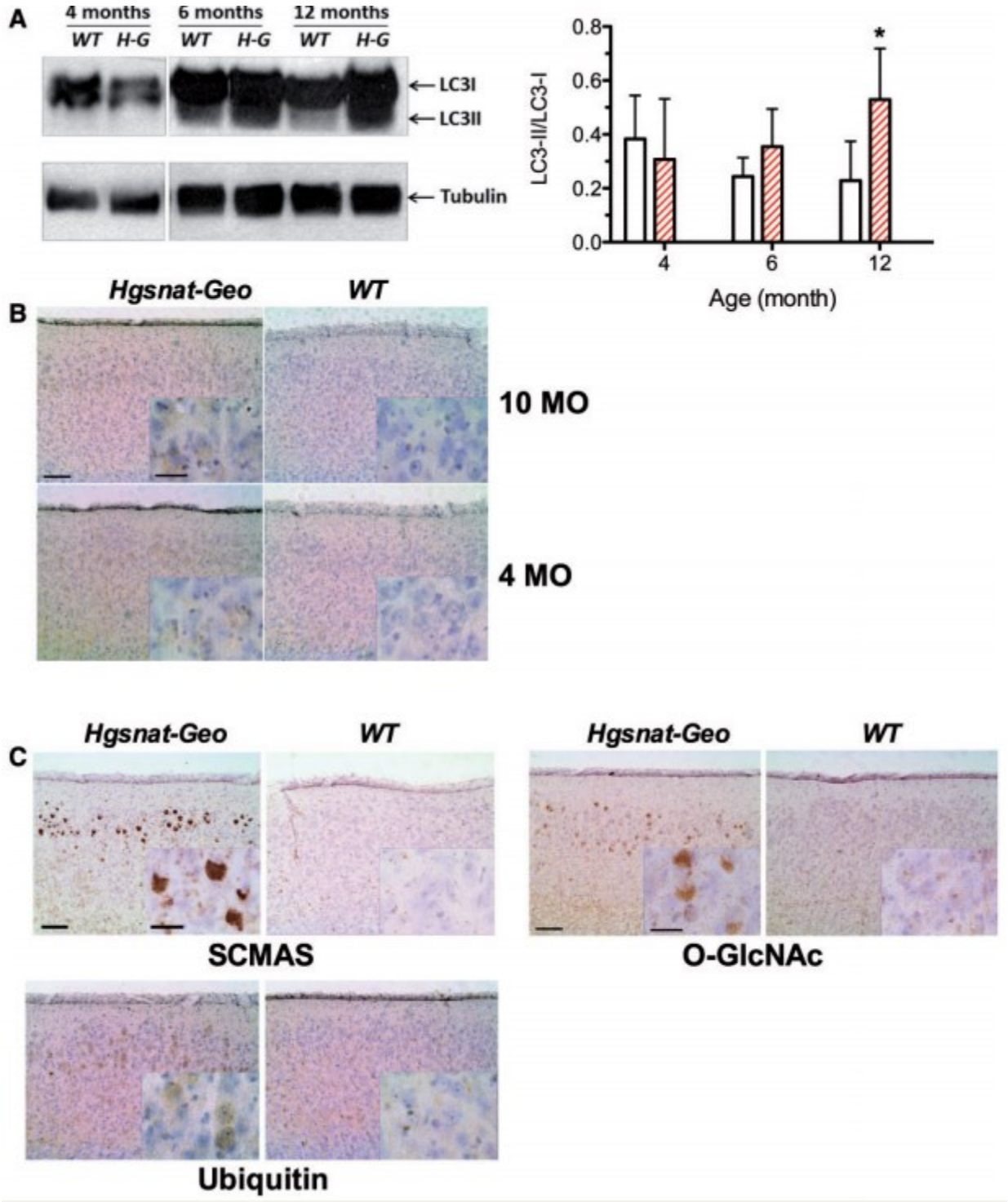

Figure 6. Brain tissues of *Hgsnat-Geo* mice show altered autophagy and lysosomal proteolysis.

A) Increased levels of LC3-II were detected in the brain tissues of *Hgsnat-Geo* ***(H-G)*** mice at the age of 6 and 10 months but not at the age of 4 months by the Western blot. Total mouse brains were

homogenized in 250 mM sucrose buffer and after removal of nuclei proteins were solubilized with 1% Triton X-100. Protein extracts were analyzed by Western blotting using antibodies specific for mouse LC3 and β-tubulin as a loading control. Panel shows representative data of three independent experiments performed with three *Hgsnat-Geo* and three wild type mice for each age. Inset graph shows ratios (means and S.D.) of signal intensities for LC3-II and LC3-I estimated with ImageQuant software. * $P < 0.05$ in unpaired two-tailed t-test.

B) LC3 staining was present in the cytoplasm of MEnt neurons of 10-month-old but not of 4-month-old *Hgsnat-Geo* mice.

C) Signs of impaired lysosomal proteolysis and ER stress in the neurons of *Hgsnat-Geo* mice. SCMAS-positive aggregates, O-GlcNAc-modified proteins and increased staining for ubiquitin were detected in MEnt neurons of 10-month-old *Hgsnat-Geo* mice. The scale bars are 100 μm. The scale bars in the inserts are 30 μm.

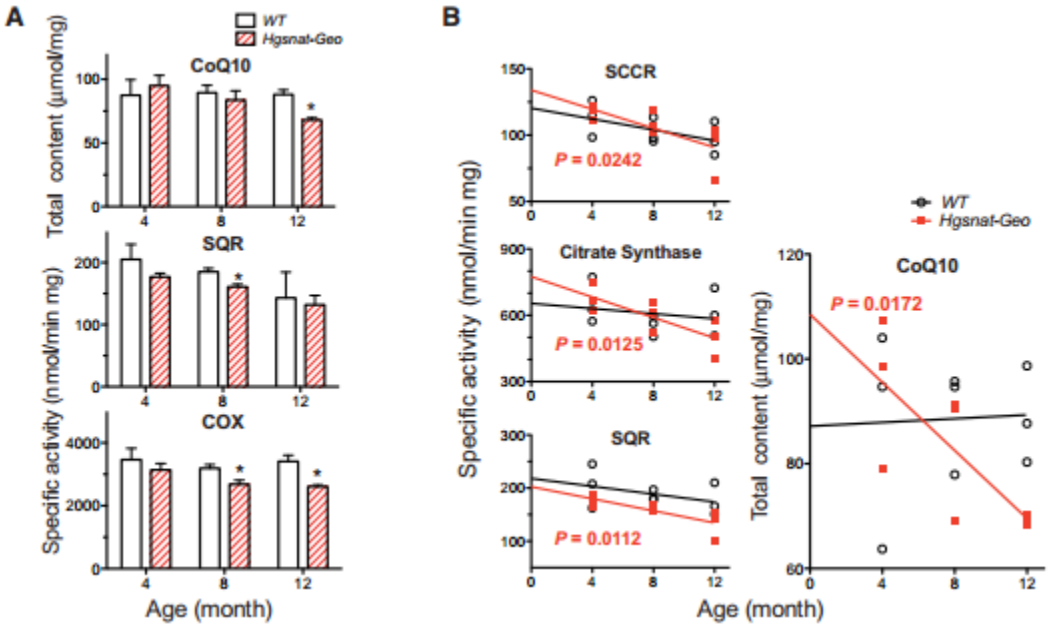

Figure 7. Partial impairment of mitochondrial oxidative phosphorylation system in the brains of *Hgsnat-Geo* mice

(A) Activity of succinate: CoQ reductase (SQR, complex II) and cytochrome c oxidase (COX, complex IV) in isolated brain mitochondria of *Hgsnat-Geo* mice are reduced as compared with age-matching wild type controls. Total content of coenzyme Q10 in brain homogenate of *Hgsnat-Geo* mice is reduced as compared with wild type controls. The data show means (±S.D.) of individual measurements. Three mice were analyzed for each age and each genotype. * $P < 0.05$ in unpaired two-tailed t-test.

(**B**) Correlation between the age and activities of succinate: CoQ reductase (SQR), succinate: cytochrome c reductase (SCCR), citrate synthase (CS), and total coenzyme Q10 content in the brain tissues of *Hgsnat-Geo* and wild type mice was analyzed by the linear regression method. For all parameters in the tissues of *Hgsnat-Geo* but not of wild type mice the slopes of linear regression lines showed a significant deviation from zero ($P < 0.05$). Three mice were analyzed for each age and each genotype.

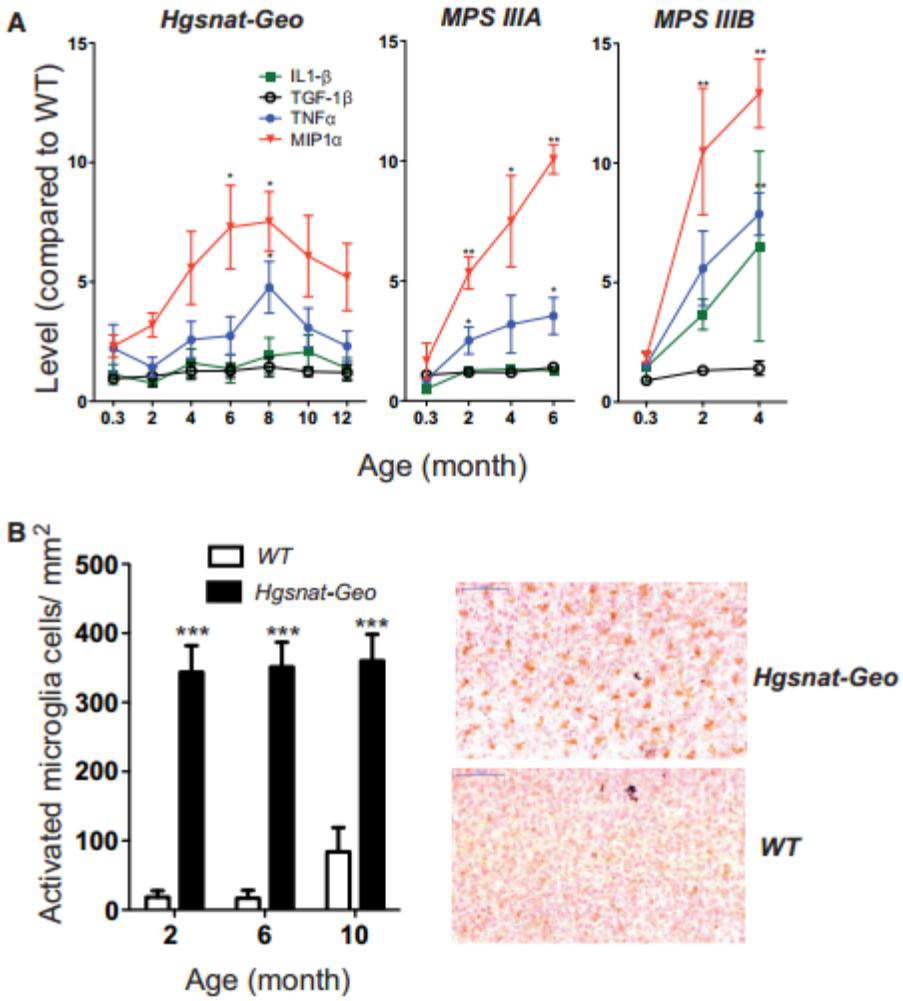

Figure 8. Brain inflammation in *Hgsnat-Geo* mice.

A) Total brain tissues of *Hgsnat-Geo* mice show progressively increased expression of inflammation markers, MIP1α (CCL3) and TNFα similar to those in MPS IIIA, but lower than those in MPS IIIB mouse models. Total RNA was isolated from whole mouse brain, reverse-transcribed to cDNA and quantification of cytokines was performed by RT-qPCR. The data show ratios of the cytokine levels in *Hgsnat-Geo* mice and those in wild type controls (both normalized for the content of *RLP32* mRNA). Data show mean values (±SD). At least three mice were analyzed for each age, sex and genotype. Two-way ANOVA was used to test differences between the mouse groups: significant differences between the mean values in Bonferroni post-test (*$P < 0.05$, ** $P < 0.001$) are shown.

B) Increased number of activated microglial cells in brain cortex of *Hgsnat-Geo* mice. 40 μm-thick sagittal brain sections of wild type and *Hgsnat-Geo* mice were stained with HPR-conjugated microglial marker isolectin B4/DAB and counter-stained with haematoxylin as described (Wilkinson *et al*., 2012). The total number of microglial cells was counted for three adjacent 0.25 mm^2 sections of somatosensory cortex. Data show mean values (±SD). Two mice were analyzed for each age, sex and genotype. ** $P < 0.001$ in unpaired two-tailed t-test.

Supporting materials:

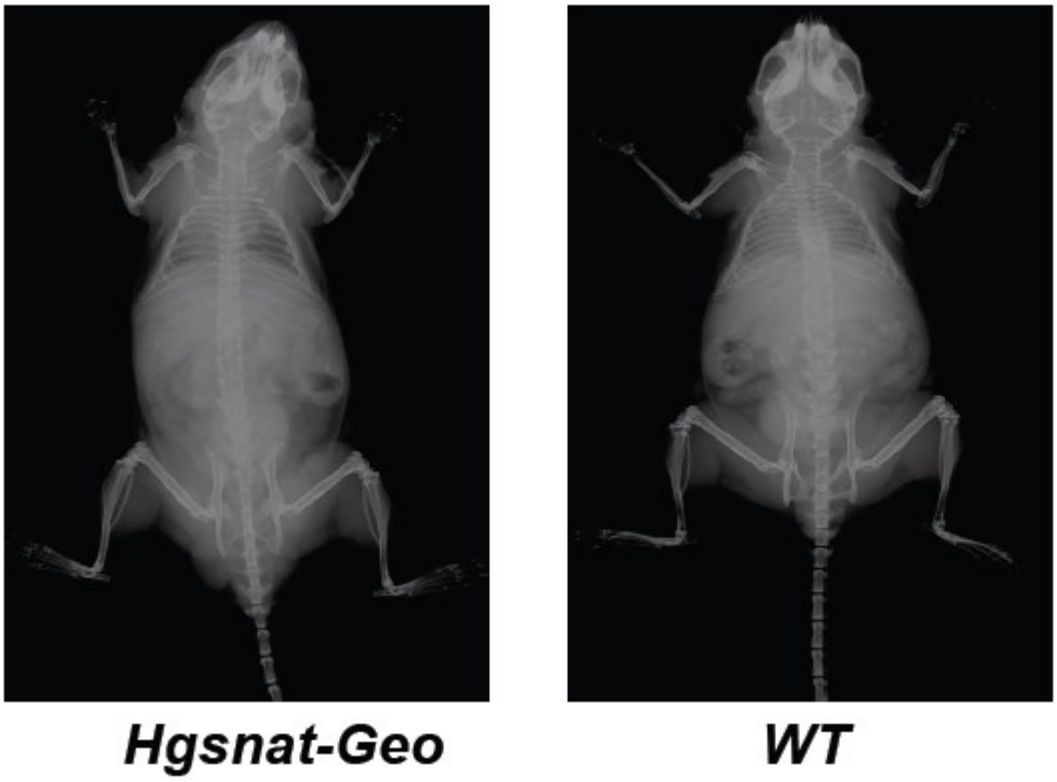

Figure S1. No bone deformation was detected by X-ray analysis of *Hgsnat-Geo* mice. Image shows representative radiographs of 2-month-old male *Hgsnat-Geo* (A) and wild type (B) mice taken with Faxitron MX2 instrument. Four mice were analyzed for each genotype.

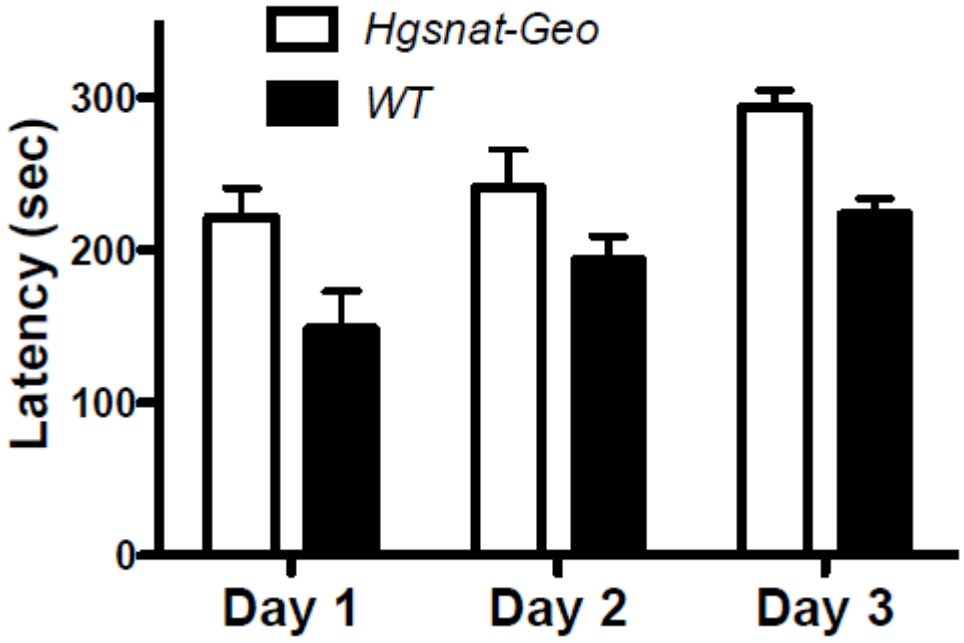

Figure S2. No significant difference was observed in accelerating Rotarod performance between 8-month-old wild type and *Hgsnat-Geo* mice.

Mice were placed on a rubber-covered rod (3.5 cm in diameter) rotating at 4 rpm. Mice were left for 3 min for adaptation and then the rotation speed was gradually increased from 4 to 40 rpm over the course of 5 min and the latency to fall (in seconds) recorded. The results are shown as means (±SD) of nine tests performed during 3 consecutive days (three tests per day). Four male and four female mice were studied for each sex and genotype. P value was calculated by t-test.

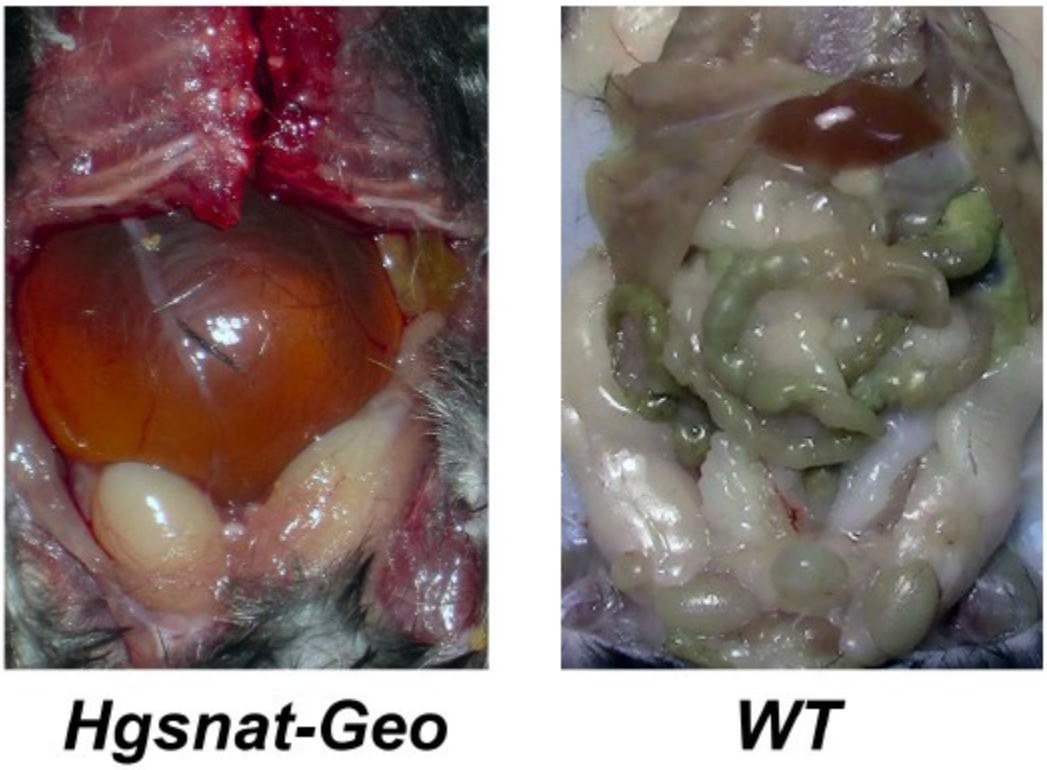

Figure S3. Representative dissection of 12-month-old *Hgsnat-Geo* mouse showing signs of urinary retention and a loss of abdominal fat. Both features are not detectable in the age-matching wild type mouse.

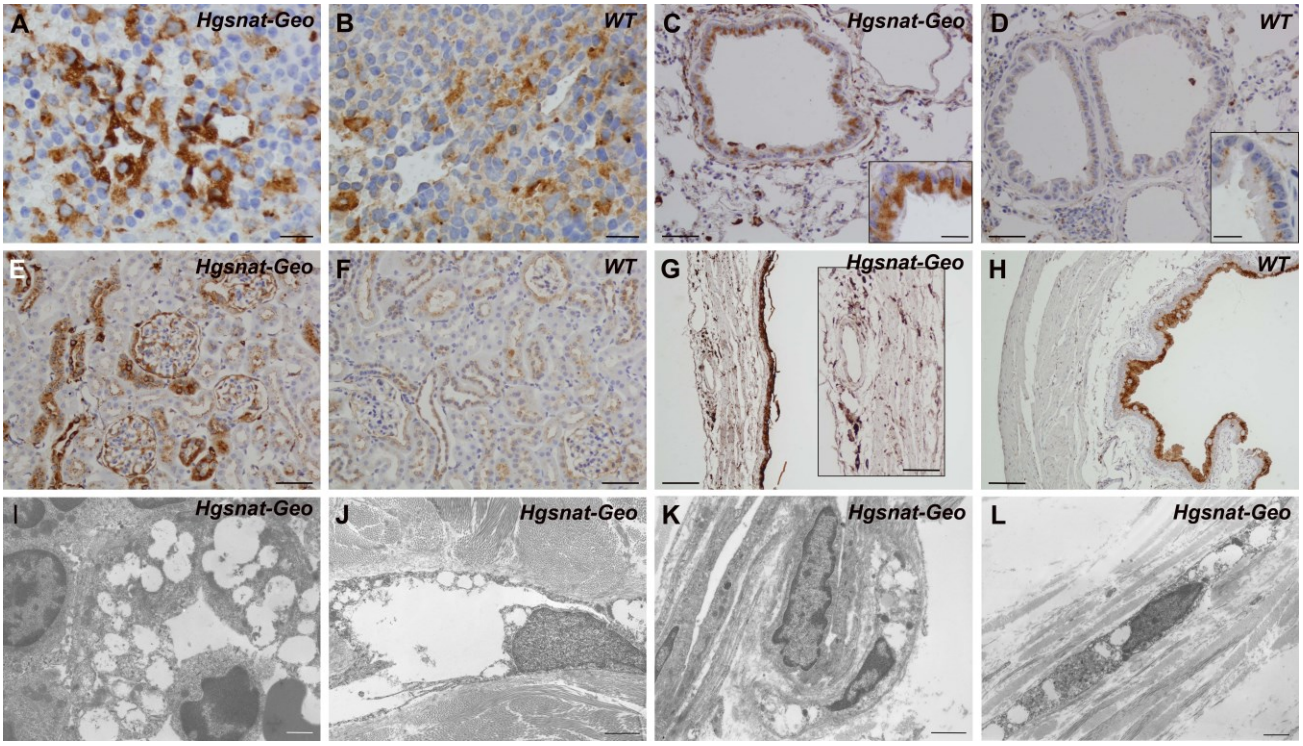

Figure S4. Profound lysosomal storage in liver of *Hgsnat-Geo* mice was detected at the optical (A-D) and ultrastructural (E-H) levels.

(A) Survey of liver parenchyma of 12-month-old *Hgsnat-Geo* mice showing microvacuolization in hepatocytes mainly in the intermediate zone and increased cellularity in liver sinusoids. Insert shows a detailed view of microvacuolization in the cytoplasm of hepatocytes and a Kupffer cell showing transformation into a foam cell. H&E stain. Bar represents 200 µm, bar in the insert, 30 µm.

(B) Immunostaining for CathD reveals expanded lysosomal system in hepatocytes and in Kupffer cells in the liver of 12-month-old *Hgsnat-Geo* mice, comparable with lysosomal storage. Insert shows a discrete signal for CathD in hepatocytes of wild type littermate control mouse. Bars represent 50 µm.

(C, D) Storage within the population of Kupffer cells and their early activation were detected in *Hgsnat-Geo* mice by immunostaining with rat monoclonal antibody (clone BM8) against Mouse Macrophage IgG2a (LS-C139904, LifeSpan Bioscience). Positively stained Kupffer cells in liver sinusoids are enlarged and increased in number in 5-month-old *Hgsnat-Geo* mice **(C)** as compared to age matching wild type mice **(D)**. Individual Kupffer cells display a storage phenotype with rounded

vacuolated cytoplasm **(C, insert)**. Kupffer cells in wild type mice are always slim, stellate or needle-shaped **(D, insert)**. Bars represent 200 µm, bars in inserts, 30 µm.

(E) Intensive lysosomal storage of soluble substances in the cytoplasm of a hepatocyte (HC) contrasting with rarely detectable storage vacuoles (marked by arrowheads) in a Kupffer cell (KC) in the sinusoid of 5-month-old *Hgsnat-Geo* mice.

(F) Higher magnification of hepatocyte (HC) cytoplasm with accumulation of vacuoles surrounded by a single limiting membrane, either electronlucent or with a sparse fine content. Structures resembling autophagic vacuoles (marked by arrows) were occasionally detected.

(G, H) Ultrastructural pattern characteristic for lysosomal storage of GAG (marked by arrowheads) was clearly detectable at 12 months in Kupffer cells (KC) **(G)** and in perisinusoidal Ito cells also containing droplets of neutral lipids in their cytoplasm **(H)**. Bars represent 1 µm.

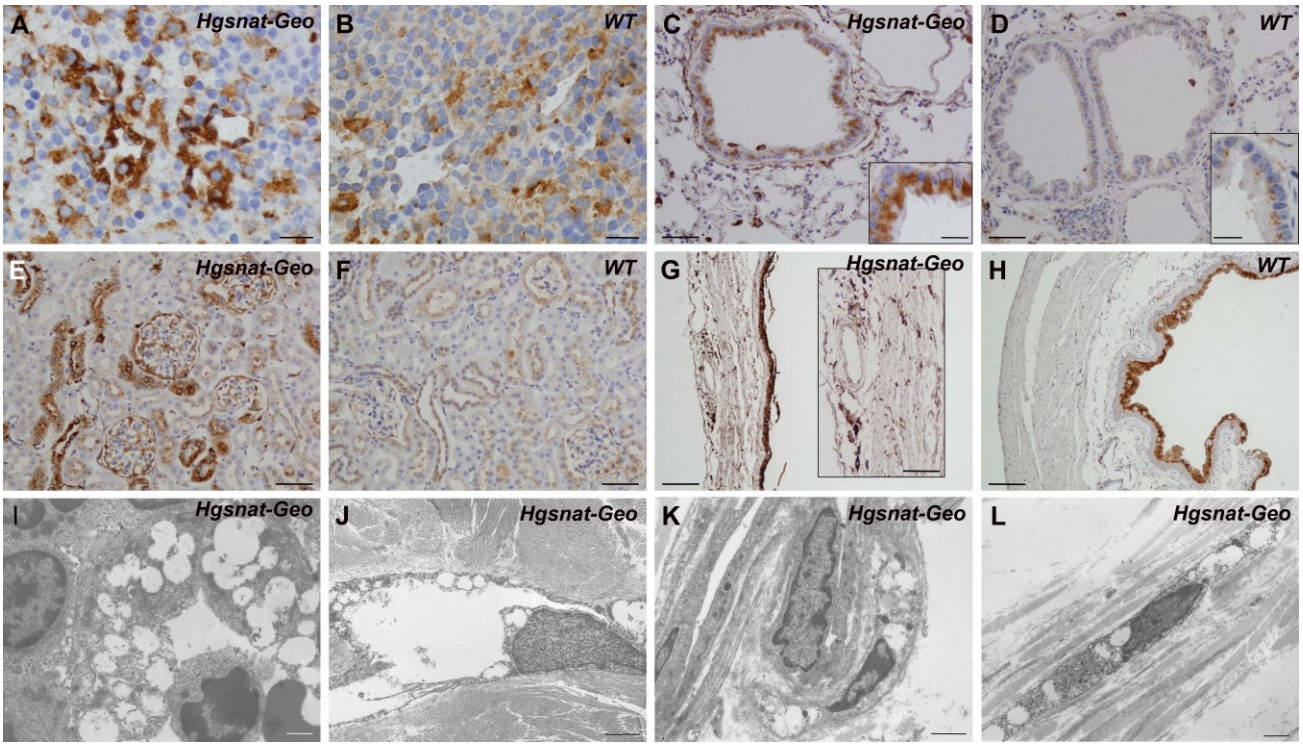

Figure S5. Widespread lysosomal storage in epithelial and mesenchymal cells in *Hgsnat-Geo* mice. CathD immunostaining of lysosomal system (A-H) and electron microscopy of selected cell types (I-L).

Lysosomal system was expanded and activated in splenic sinus endothelium **(A)** and less so in bronchial respiratory epithelium (**C**), as well as in distal tubules, collecting ducts and glomeruli of renal cortex (**E**) of 12-month-old *Hgsnat-Geo* mice. Tissues of age-matching wild type animals **(B, D** and **F)** do not show these features. (**G**) A thin wall of distended urinary bladder of a 12-month-old *Hgsnat-Geo* mouse with a sparse presence in lamina and muscularis propria and adventitia of cells with expanded cytoplasm strongly positive for CathD. (**H**) Urinary bladder of age-matching wild type animal has normal wall thickness and structure. Inserts show detailed views of the cells.

Electronlucent vacuoles surrounded by single membranes indicative of lysosomal storage of soluble material were detected in splenic sinus endothelium (**I**), skin vascular endothelial cells (**J**), perivascular pericytes (**K**) and fibroblasts (**L**) of 12-month-old *Hgsnat-Geo* mice.

Bars in A, B and Insert C represent 30 μm, bars in C-F and Insert G, 100μm, bars in G and H, 200 μm. Bars in I and L represent 1 μm, bars in J and K, 2 μm.

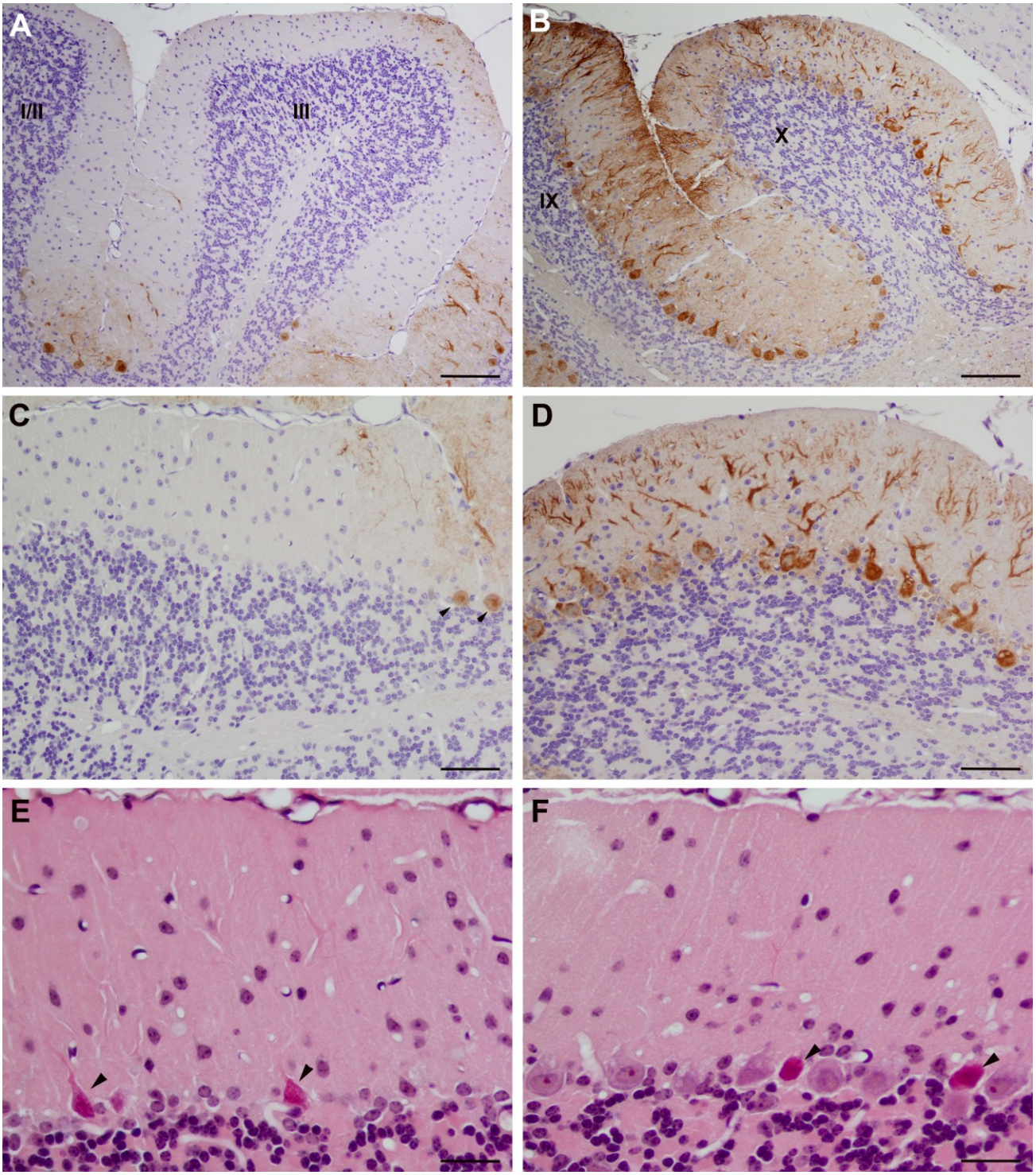

Figure S6. Purkinje cell loss in the anterior cerebellar lobe of *Hgsnat-Geo* mouse at the age of 12 months.

(**A-D**) Calbindin immunostaining in the cerebellar cortex. Staining for Purkinje cells is almost absent in lobules I-III (**A**) when compared to remaining calbindin staining in lobules IX and X (**B**). Higher

magnification of cerebellar cortex shows an exceptional presence of weakly positive Purkinje cells (marked by arrowheads) in the lobule III (**C**) and a substantially preserved Purkinje cell layer in the lobule X (**D**). Bars in A and B represent 200 μm, bars in C and D, 100 μm. (**E-F**) Details of the Purkinje cells layer, H&E staining. Purkinje cells are largely absent in the lobule III (**E**) in comparison to almost contiguous monolayer of Purkinje cells in the lobule X (**F**). Degenerating neurons with a shrunken condensed cytoplasm and nuclei are marked by arrowheads. Bars represent 50 μm.

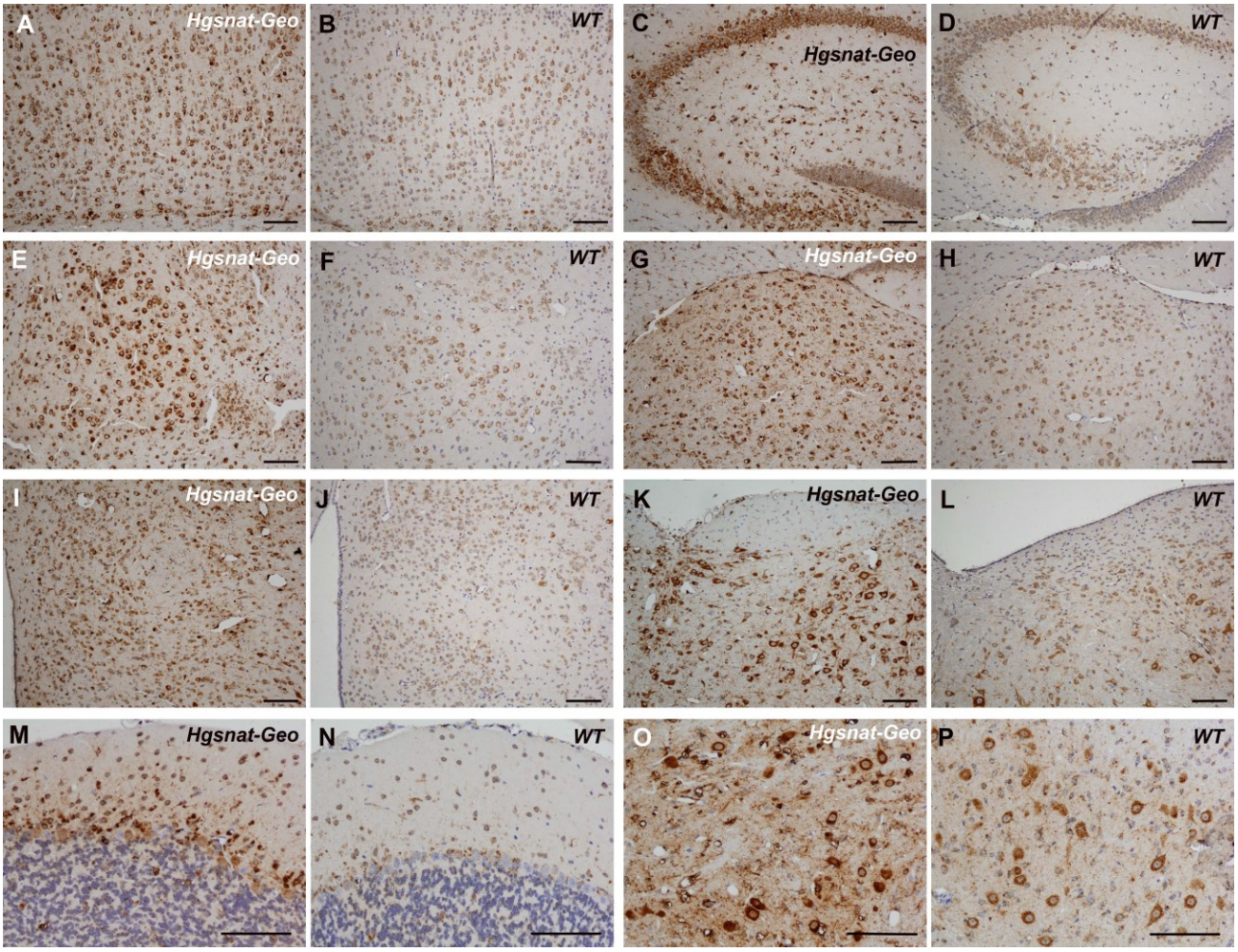

Figure S7. Increased CathD immunostaining in neurons compatible with lysosomal storage in *Hgsnat-Geo* mice as compared with relatively weak staining in wild type littermates was observed in in neocortex (**A, B**), hippocampus (**C, D**), amygdala (**E, F**), thalamus (**G, H**), hypothalamus (**I, J**),

pons (**K, L**), cerebellar cortex (**M, N**) and cerebellar nuclei (**O, P**). Panels **A-L** show brains of 12-month-old *Hgsnat-Geo* and wild type mice; panels **M-P** show brains of mice at the age of 5 months before extensive degeneration of Purkinje cells is detected. Bars represent 100 μm.

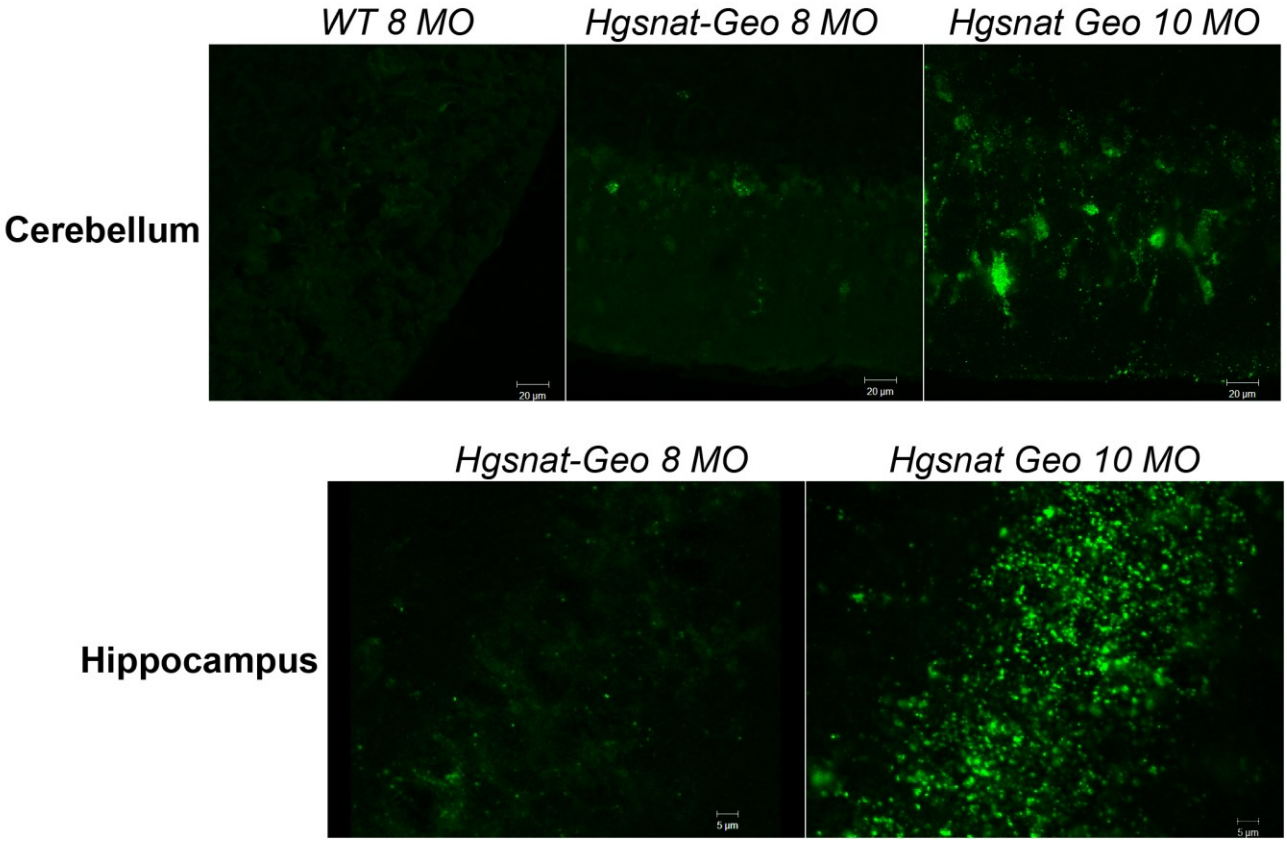

Figure S8. Progressive accumulation of G_{M2} ganglioside was detected in the hippocampus and cerebellum of *Hgsnat-Geo* mice. Bars represent 20 μm (cerebellum) and 5 μm (hippocampus).

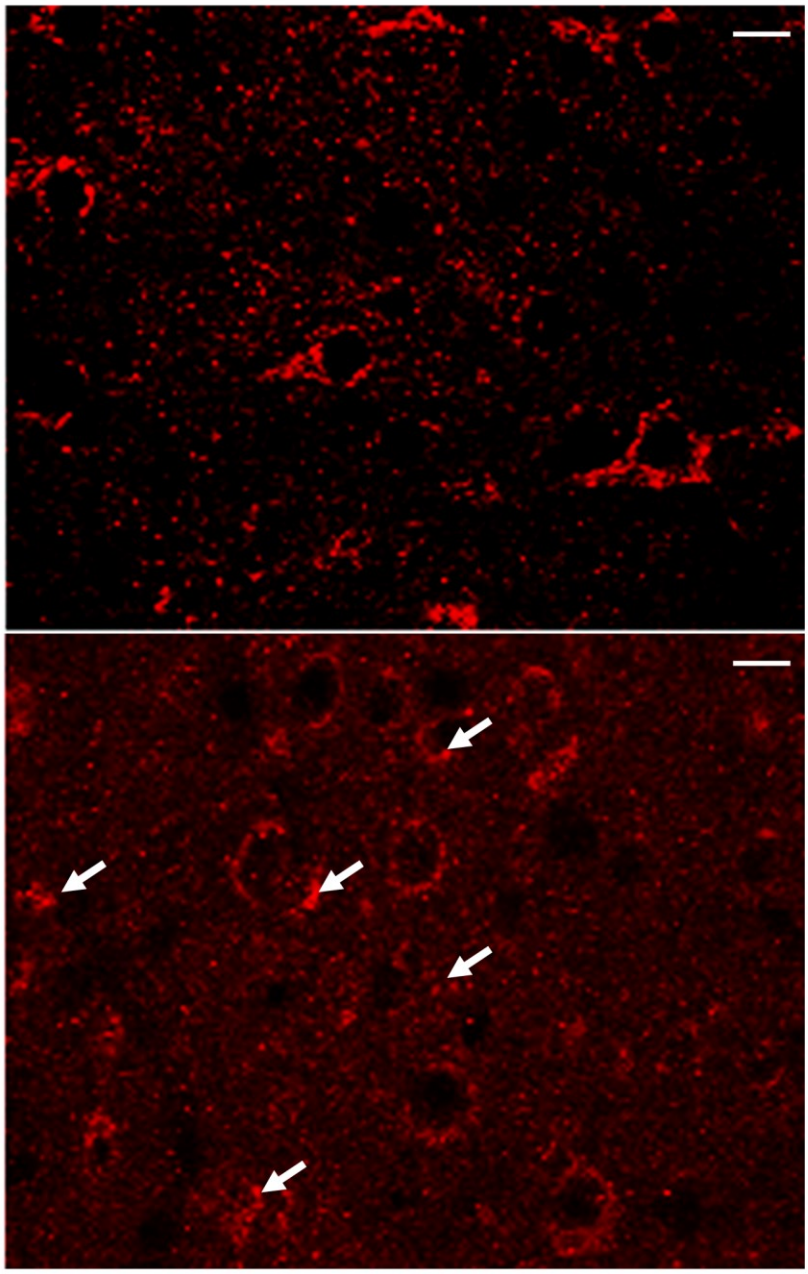

Figure S9. Mitochondrial network show signs of disorganization in cortical neurons of *HGSNAT-Geo* mice. Forty μm-thick sagittal brain sections of 8-month-old wild type and *HGSNAT-Geo* mice were stained with mitochondrial marker, cytochrome c oxidase subunit 4 (Cox4). Slides were studied on a Zeiss LSM510 inverted confocal microscope. Arrows show collapsed mitochondria in neurons of *Hgsnat-Geo* mouse.

Panels show representative images of at least 30 studied for 3 *Hgsnat-Geo* and 3 wild type mice for each age. Bars represent 10 μm.

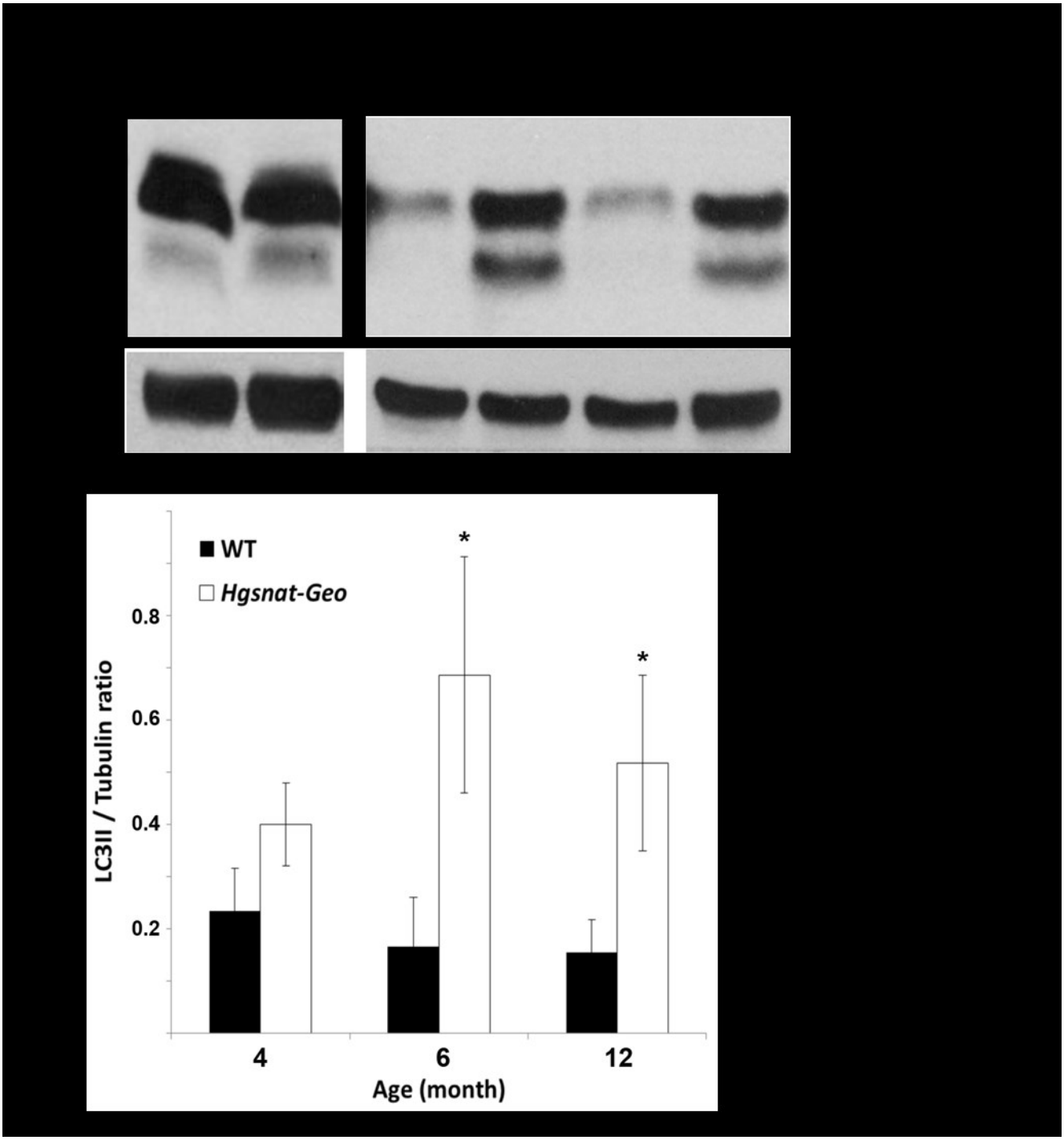

Figure S10. Increase of LC3-II in liver tissues of *Hgsnat-Geo* mice suggestive of impaired autophagy. Livers of 4, 6 and 12-month-old *Hgsnat-Geo* and wild type mice were homogenized in

RIPA buffer. Protein extracts were analyzed by Western blot using antibodies specific for mouse LC3 and β-tubulin as a loading control.

A. Panel shows representative data of 3 independent experiments.

B. Graph shows ratios (means and S.D.) of signal intensities for LC3-II and β-tubulin estimated with ImageQuant software. Bars show mean values ±S.D., n=3. *$p<0.05$ in unpaired two-tailed t-test.

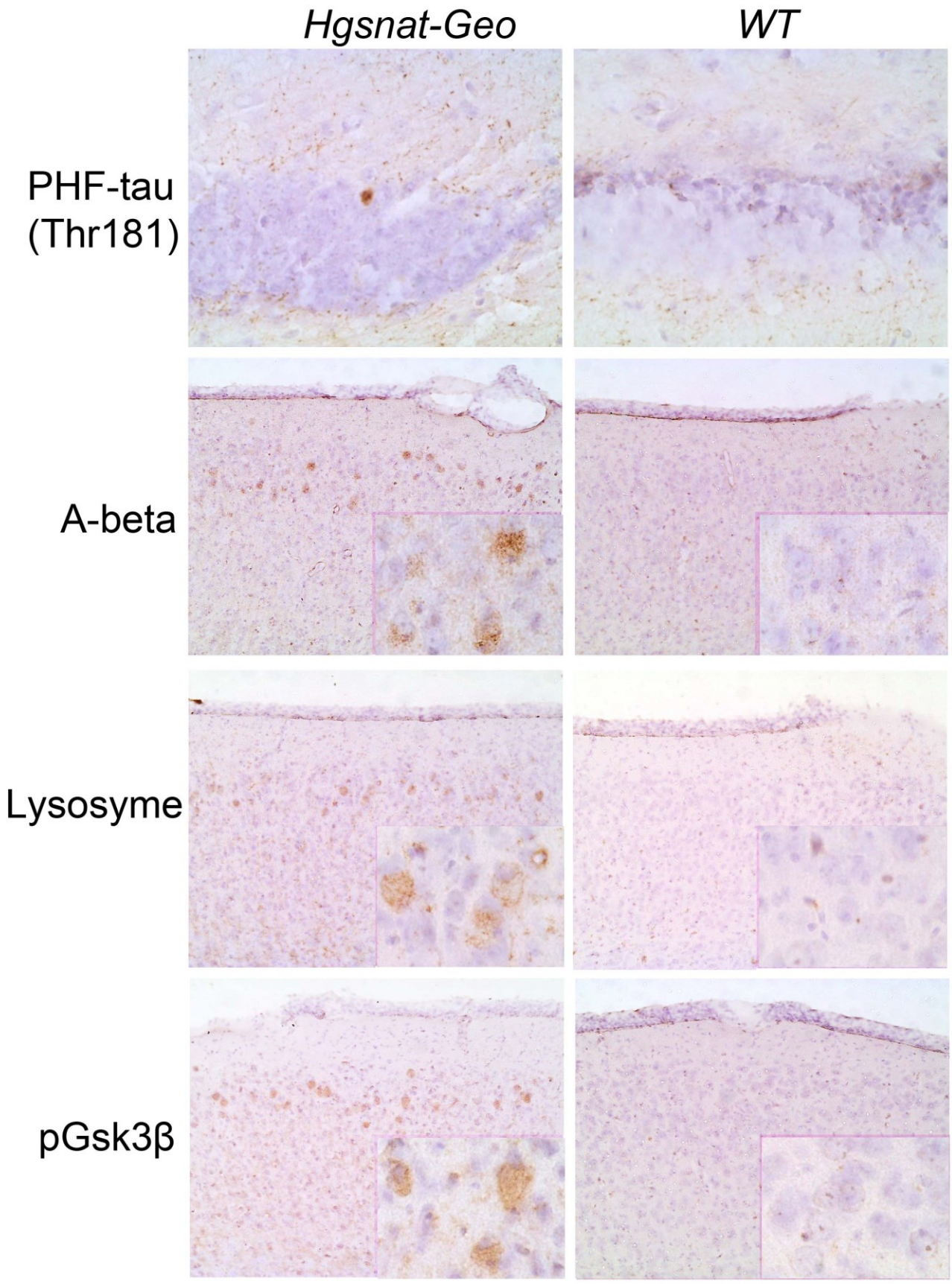
Hgsnat-Geo
WT
PHF-tau (Thr181)
A-beta
Lysosyme
pGsk3β

Figure S11. Accumulation of brain protein markers of neurodegeneration associated with dementia: lysozyme, beta amyloid (A-beta), and Ptau kinase Gsk3β in MEnt and phosphorylated tau (PHF-tau Thr181) in dentate gyrus of 10-month-old *Hgsnat-Geo* mice. Bars represent 100 μm; bars in the inserts, 30 μm.

Supplemental video 1. Video recording of 8-month-old male *Hgsnat-Geo* mouse showing loss of coordination.

Supplemental video 2. Video recordings of 8-month-old female wild type (a) and *Hgsnat-Geo* (b) mice in the open field test. *Hgsnat-Geo* mouse shows signs of hyperactivity and reduced anxiety compared to wild type mouse.